

Extrusion-based additive manufacturing of Mg-Zn/bioceramic composite scaffolds

Dong, J.; Lin, P.; Putra, N. E.; Tümer, N.; Leeflang, M. A.; Huan, Z.; Fratila-Apachitei, L. E.; Chang, J.; Zadpoor, A. A.; Zhou, J.

DOI

[10.1016/j.actbio.2022.08.002](https://doi.org/10.1016/j.actbio.2022.08.002)

Publication date

2022

Document Version

Final published version

Published in

Acta Biomaterialia

Citation (APA)

Dong, J., Lin, P., Putra, N. E., Tümer, N., Leeflang, M. A., Huan, Z., Fratila-Apachitei, L. E., Chang, J., Zadpoor, A. A., & Zhou, J. (2022). Extrusion-based additive manufacturing of Mg-Zn/bioceramic composite scaffolds. *Acta Biomaterialia*, 151, 628-646. <https://doi.org/10.1016/j.actbio.2022.08.002>

Important note

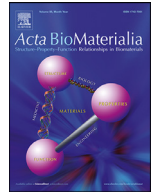
To cite this publication, please use the final published version (if applicable).
Please check the document version above.

Copyright

Other than for strictly personal use, it is not permitted to download, forward or distribute the text or part of it, without the consent of the author(s) and/or copyright holder(s), unless the work is under an open content license such as Creative Commons.

Takedown policy

Please contact us and provide details if you believe this document breaches copyrights.
We will remove access to the work immediately and investigate your claim.



Full length article

Extrusion-based additive manufacturing of Mg-Zn/bioceramic composite scaffolds



J. Dong^{a,*}, P. Lin^b, N.E. Putra^a, N. Tümer^a, M.A. Leeflang^a, Z. Huan^c, L.E. Fratila-Apachitei^a, J. Chang^c, A.A. Zadpoor^a, J. Zhou^a

^a Department of Biomechanical Engineering, Delft University of Technology, Delft 2628 CD, the Netherlands

^b Department of Engineering Structures, Delft University of Technology, Delft 2628 CN, the Netherlands

^c Shanghai Institute of Ceramics, Chinese Academy of Sciences, 1295 Dingxi Road, Shanghai 200050, China

ARTICLE INFO

Article history:

Received 26 May 2022

Revised 9 July 2022

Accepted 1 August 2022

Available online 5 August 2022

Keywords:

3D printing

Material extrusion

Magnesium

Composite

Scaffold

ABSTRACT

The treatment of femoral nonunion with large segmental bone defect is still challenging. Although magnesium alloys have been considered potential materials for such a treatment, their application is limited by their fast degradation. Adding bioceramic particles into magnesium to form Mg-matrix composites is a promising strategy to adjust their biodegradation rates and to improve their mechanical properties and cytocompatibility further. Here, we developed an extrusion-based additive manufacturing technique to fabricate biodegradable Mg-Zn/bioceramic composite scaffolds *ex-situ*. Inks carrying a Mg-Zn powder and 5, 10 and 15% β -tricalcium phosphate (TCP) powder particles were investigated regarding the dispersion of β -TCP particles in the inks and viscoelastic properties. Optimally formulated inks were then employed for subsequent 3D printing of porous composite scaffolds. The *in vitro* biodegradation rate of the scaffolds containing 5% β -TCP decreased to 0.5 mm/y, which falls within the range desired for critical-sized bone substitution. As compared to the monolithic Mg-Zn scaffolds, the elastic moduli and yield strengths of the composite scaffolds were much enhanced, which remained in the range of the cancellous bone properties even after 28 d of *in vitro* degradation. The Mg-Zn/5TCP and Mg-Zn/10TCP scaffolds also exhibited improved biocompatibility when cultured with preosteoblasts, as compared to Mg-Zn scaffolds. In addition, the ALP activity and mineralization level of the composite scaffolds were much enhanced in the extracts of the composite scaffolds. Taken together, this research marks a great breakthrough in fabricating porous Mg-matrix composite scaffolds that meet several design criteria in terms of appropriate biodegradation rate, mechanical properties, and bioactivity.

Statement of significance

The treatment of posttraumatic femoral nonunion with large segmental bone defect is still challenging. In this study, we developed a multi-material extrusion-based additive technique to fabricate porous Mg/bioceramic composite scaffolds for such a treatment. The technique allowed for the fine-tuning of printable inks to optimize the dispersion of micro-sized particles. The relative densities of the struts of the fabricated composite scaffolds reached 99%. The added bioceramic particles (β -TCP) exhibited proper interfacial bonding with the Mg alloy matrix. The porous Mg-based composite possessed desired biodegradability, bone-mimicking mechanical properties throughout the *in vitro* biodegradation period and improved bioactivity to bone cells. These results demonstrated great prospects of extrusion-based 3D printed porous Mg materials to be developed further as ideal biodegradable bone-substituting materials.

© 2022 The Author(s). Published by Elsevier Ltd on behalf of Acta Materialia Inc.

This is an open access article under the CC BY-NC-ND license

(<http://creativecommons.org/licenses/by-nc-nd/4.0/>)

1. Introduction

The treatment of posttraumatic femoral nonunion with large segmental bone defect remains a great challenge in orthopedics [1]. Current therapeutic approaches to such bone defect repair

* Corresponding author.

E-mail address: J.Dong-5@tudelft.nl (J. Dong).

include the implantation of autologous, allogeneic, or synthetic grafts, as well as the use of distraction osteogenesis techniques. However, all the approaches mentioned above have their own disadvantages and limitations [2]. Magnesium and its alloys have been considered promising implant materials to be used for the regeneration of such critical-sized bone defects, because of their biodegradability, favorable mechanical properties, and osteogenic potential [3]. However, the application of Mg and its alloys in orthopedics is still limited because of their high corrosion rates, resulting in the generation of a large amount of hydrogen gas that could trigger acute inflammatory responses and formation of gas voids [4]. The release of potentially toxic ions from the alloying elements along with fast biodegradation can also occur. Numerous studies have indicated the strong need for developing Mg-based materials with adjustable biodegradation rates and desirable biocompatibility to meet the requirements for bone repair [5–8]. Although surface modification can potentially solve these problems, it only helps to delay the start of corrosion. Indeed, the acceleration of corrosion often occurs when the coating breaks down [9]. Another promising approach is to form Mg-based composites through the addition of bioceramic particles to Mg [10]. Bioceramics based on calcium phosphate, such as hydroxyapatite (HA) and β -tricalcium phosphate (β -TCP), are particularly interesting for bone repair applications due to their similarity to natural bone in composition, and their osteoinductive and osteoconductive properties [10]. Unlike HA that has a very low solubility in the physiological environment, β -TCP exhibits a suitable biodegradation profile with a proper match with the rate of bone tissue regeneration [5]. It has been found that the addition of β -TCP to Mg alloys is, indeed, effective in enhancing their strength, stabilizing their corrosion rate, and improving their cytocompatibility [11–13]. With these findings in mind, researchers have made great efforts to fabricate Mg/ β -TCP composites with various techniques. Both liquid-state processing techniques, such as stir casting [14,15] and liquid infiltration [13], and solid-state processing methods, such as powder metallurgy [11,16] and friction stir processing [17], have been applied for the fabrication of such composites. However, none of these techniques is capable of fabricating complex 3D architectures with fully interconnected porous networks that are of great importance for bone substitutes [18]. Indeed, an interconnected porous structure affords the bone substitute with favorable permeability and large surface area, thereby facilitating cell proliferation and differentiation [19,20].

In recent years, additive manufacturing (AM) has emerged as a powerful technique for the precise, free-form fabrication of orthopedic implants with complex internal and external macro- and micro-architectures [21]. The recent advances in AM techniques have also enabled the production of Mg-based composite bone substitutes [22]. However, the available studies are limited both in number and scope. Only a few research groups have succeeded in employing powder bed fusion (PBF) AM techniques for the fabrication of Mg-bioceramic composites [23–26]. These studies are still in their infancy and are limited to bulk Mg-based composites, instead of porous scaffolds that are preferable for bone regeneration. High-level porosity and the agglomeration of ceramic particles, corresponding to undesirable defects and compositional variations, respectively, are common observations in these studies due to the sharp differences between the magnesium and bioceramic in the whole range of physical and chemical properties, such as melting and evaporation temperatures, crystal structure, wettability, reflectivity, thermal expansion coefficient, and chemical reactivity [22]. In addition, concerns have been raised about operating PBF AM to fabricate Mg-based alloys or composites, considering the high flammability of Mg powder [27]. Most laboratories try to avoid this risk. A laser-free AM technique would be a safer and more promising alternative.

Extrusion-based AM of such composites is a room temperature technique that works by continuously pushing a viscoelastic ink, composed of a metal powder, a ceramic powder, and a binder system through a nozzle to build a 3D structure based on CAD design, followed by debinding and sintering [28]. This technique effectively avoids the problems associated with PBF AM techniques. Another advantage of the ink extrusion-based AM is that various components can be flexibly added into the ink to create multi-functional bone-substituting materials [29,30]. Even though this production technique has been explored to fabricate porous Mg and Mg alloy bone substitutes [28,31,32], no reports have appeared in the literature reporting the fabrication of Mg-bioceramic composite scaffolds.

Here, we used an ink extrusion-based AM technique to fabricate Mg-Zn/ β -TCP composite scaffolds. As the scaffolds made of a Mg-Zn alloy exhibited a very promising biodegradation rate, despite their cytotoxicity [32], the Mg-Zn alloy was chosen as the matrix. We hypothesized that the addition of β -TCP into the scaffolds would improve both the cytocompatibility and bioactivity of the Mg-Zn scaffolds. The main challenge lies in achieving uniform dispersion of micro-sized bioceramic particles in the metal matrix, considering their large surface areas and the strong van der Waals forces between dispersed particles [6]. The agglomeration of incorporated bioceramic particles has, indeed, been found to cause the formation of pores and defects, deteriorating the corrosion behavior and mechanical properties of the resulting composite [33]. To minimize such effects, two fabrication processes may be combined. For example, conventional powder metallurgy may be followed by hot extrusion [34–39] while high-shear solidification may be combined with equal channel angular extrusion [40,41] or with high-pressure die casting [15]. In the present research, we tried to overcome this challenge by developing an optimized binder system for preparing inks with well-dispersed particles, which could greatly reduce the processing complexity of the composites, as compared with the other solutions mentioned above. At the same time, rheological properties of the inks should be finely tuned in order to guarantee printability. In other words, it was critical to develop inks with well-dispersed solid particles (both metal and ceramic) and also with viscoelastic behavior necessary for the printability of these inks.

Herein, we report, for the first time, the successful fabrication of Mg-based composite scaffolds with 5, 10, and 15 wt% of β -TCP particles using ink extrusion-based AM. First, we present the results of our study regarding ink development. Then, we characterize the 3D printed composite scaffolds in terms of their microstructure, *in vitro* biodegradation, biodegradation-dependent mechanical properties. Finally, we use preosteoblasts to assess the cytocompatibility and bioactivity (*i.e.*, cell viability and osteogenic response) of the developed specimens. The successful employment of ink extrusion-based 3D printing to fabricate porous Mg alloy/bioceramic composites marks the emergence of a new category of porous Mg biomaterials potentially to be used in orthopedics and it also devises another strategy for achieving uniform dispersion of micro-sized reinforcing particles in porous composites.

2. Materials and methods

A schematic illustration of the composite fabrication steps, including ink preparation, structural design, 3D printing, debinding, and sintering is presented in Fig. 1.

2.1. Ink preparation and characterization

2.1.1. Ink preparation

A pre-alloyed spherical Mg-Zn alloy powder (95.6 wt% Mg, 4.1 wt% Zn and 0.3 wt% impurities: Al and Ca, Tangshan Wei-

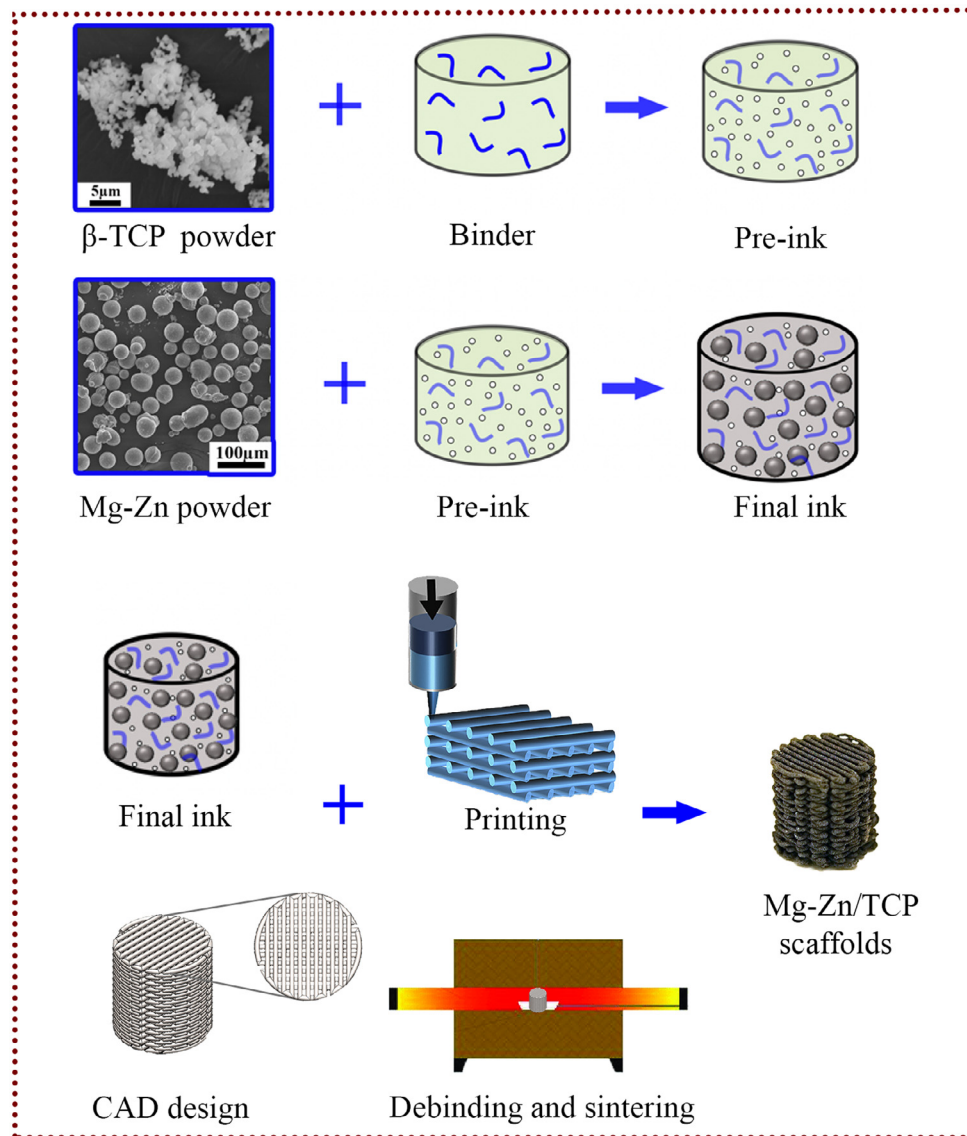


Fig. 1. A schematic illustration of the fabrication steps of the composite scaffolds.

hao Magnesium Powder Co., China) with a median particle size of 37.7 μm (standard deviation of 6.6 μm , Fig. 1), and a β -TCP powder with an average particle size of 5.3 μm (standard deviation of 8.9 μm , Fig. 1) were used as the starting materials for the preparation of inks. A binder system with the polyisobutylene polymer ($M_w \sim 500,000$, Sigma Aldrich, Germany) in hexane was chosen.

Prior to the addition of the Mg-Zn powder, the β -TCP powder particles were mixed with 93, 95, and 97 vol.% binders (denoted as 93, 95, and 97% pre-inks) to evaluate the homogeneity of the dispersions with a scanning electron microscope (SEM, JSM-IT100, JEOL). The pre-inks were mixed for 2 h at room temperature using a magnetic stirrer at a speed of 100–150 rpm. The quadrat method was used for the quantification of the distribution of β -TCP particles in the binder solution [42]. The obtained SEM images were divided into 35 contiguous quadrats. To minimize the edge effects, only the particles that were inside and in contact with the left and bottom sides of each quadrat were counted. The number of β -TCP particles, N_q , in each quadrat was counted using ImageJ (National Institutes of Health, USA) and was then manually checked. The degree of the asymmetry of a statistical distribu-

tion around the mean number was quantified by its skewness, β , as [43]:

$$\beta = \frac{q}{(q-1)(q-2)} \sum \left(\frac{N_{qi} - N_q^{mean}}{\sigma} \right)^3 \quad (1)$$

where q is the total number of the quadrats, N_{qi} is the number of the β -TCP particles in the i th quadrat ($i = 1, 2, \dots, q$), N_q^{mean} is the mean number of the β -TCP particles per quadrat, and σ is the standard deviation of the N_q distribution. An increase in the β value indicates an increased degree of agglomeration of the β -TCP particles.

Different groups of inks were then prepared by adding the Mg-Zn powder to the prepared 93, 95, and 97% pre-inks, with mass ratios of 95:5, 90:10, and 85:15 (i.e., volume ratios of 97:3, 94:6, and 91:9) between the Mg-Zn powder and β -TCP powder, respectively. The mixing process for these inks was the same as that for the pre-inks, as described above. The inks were further optimized, based on their rheological properties (as described below) for printing Mg-Zn/5 wt.% β -TCP, Mg-Zn/10 wt.% β -TCP, and Mg-Zn/15 wt.% β -TCP composite scaffolds, hereafter denoted as Mg-Zn/5TCP, Mg-Zn/10TCP, and Mg-Zn/15TCP, respectively. Mixing was

performed in a glove box to prevent the oxidation of Mg-Zn powder particles.

2.1.2. Rheological characterization

The rheological properties of the prepared inks were determined using a rheometer (Physica MCR 301, Anton Paar, Germany). The inks were loaded onto a pair of parallel plates (diameter = 25 mm, distance = 1 mm). Shear stress-viscosity measurements were performed with stresses ranging between 1 and 10,000 Pa and the linear viscoelastic range was defined. Rotational shear rate ramps varying between 0.1 and 1000 s^{-1} were applied to the inks and the shear rate-viscosity curves were obtained. In addition, creep-recovery tests were performed to evaluate the viscoelastic properties of the inks. A constant shear stress ($\tau = 10$ Pa) selected within the linear viscoelastic range was applied for 60 s and the resulting strain was recorded. The stress was then removed, and the strain was measured for another 180 s. The compliance J was defined from the ratio of the measured strain to the applied stress. The recovery ability of the inks could then be determined as:

$$R = \frac{J_{max} - J_{\infty}}{J_{max}} \quad (2)$$

where R is the degree of recovery of the ink, and J_{max} and J_{∞} are the compliances at the end of the creep and the recovery tests, respectively.

2.2. Composite scaffold fabrication

A porous cylindrical structure (having a diameter of 12.38 mm and a height of 12.64 mm, designed for compressive tests according to the ISO 13314 standard) with a lay-down pattern of $0^{\circ}/90^{\circ}/0^{\circ}$ was designed using the GeSim custom software (Fig. 1). The structure had the following characteristics: struts size = 580 μm , strut spacing = 360 μm , and relative density = 62.2%, and layer number = 27. The adoption of the strut size was based on the considerations of the biodegradation of the scaffolds and the ability of the binder to escape during thermal debinding [31]. A pore size of 360 μm was chosen because it was found earlier that implants with pores larger than 300 μm were favorable for bone ingrowth [44]. The prepared inks were loaded into syringes (EFD, Nordson, Germany) with a 580 μm tapered nozzle (art. No. 500890, EFD, Vieweg, Germany) and were then extruded at room temperature using a 3D Bioscaffolder 3.2 printer (GeSiM Bio-instruments, Germany) under an applied pressure of 140–160 kPa and at a printing speed of 10 mm/s. The 3D printing strategy regarding the adoption of printing pressure and speed can be found in our previous publication [28].

To investigate the effect of the β -TCP dispersion in the binder on the quality of the 3D printed composite materials, Mg-Zn/10 wt.% β -TCP-containing inks with 93, 95, and 97% pre-inks were prepared and extruded through the printer nozzle. The printed struts and the cross-section of the used nozzles were imaged with SEM. In addition, to check the printability of the inks, Mg-Zn/5TCP, Mg-Zn/10TCP, and Mg-Zn/15TCP composite scaffolds printed with 93, 95, and 97% pre-inks were imaged using an optical microscope (OM, VH-Z250R, Keyence Corp., USA). After optimization based on the homogeneity of β -TCP dispersion and the printability, Mg-Zn/5TCP, Mg-Zn/10TCP, and Mg-Zn/15TCP composite scaffolds were printed with the optimized inks, using the Bioscaffolder. The powder loading volume fractions of the optimized inks were 48 vol% for the Mg-Zn/5TCP ink, 47 vol% for the Mg-Zn/10TCP ink, and 46 vol% for the Mg-Zn/15TCP ink.

The as-printed Mg-Zn/ β -TCP composite scaffolds were dried overnight, followed by debinding and sintering in a tube furnace (STF16/180, Carbolite Gero Ltd., UK) under highly pure argon

flow (purity=99.9999%; inlet pressure = 1 bar). The printed Mg-Zn/5TCP samples were heated from room temperature to 600 $^{\circ}C$ at a heating rate of 2 $^{\circ}C/min$ and the printed Mg-Zn/10TCP and Mg-Zn/15TCP samples were heated to 620 and 640 $^{\circ}C$, respectively, at a heating rate of 1 $^{\circ}C/min$. The dwelling time of all the samples was 1 h, followed by furnace cooling. The as-sintered composite scaffolds were ultrasonically cleaned in acetone and isopropyl alcohol sequentially for 10 min each, prior to subsequent investigations.

2.3. Characterization of the composite scaffolds

The porous structures of the Mg-Zn/TCP composite scaffolds were observed using SEM, and the width and spacing of the struts were measured. The absolute porosities of the as-sintered composite scaffolds were calculated using the dry weighing method as:

$$\varphi = \left(1 - \frac{m}{V_{bulk} \rho_{Mg-Zn/TCP}} \right) \times 100\% \quad (3)$$

where φ is the absolute porosity of the as-sintered composite scaffold [%], m is the mass of the as-sintered composite scaffold [g], V_{bulk} is the bulk volume [cm^3], and $\rho_{Mg-Zn/TCP}$ is the theoretical density of the Mg-Zn/TCP composite material (i.e., 1.78 g/cm^3 for Mg-Zn/5TCP, 1.82 g/cm^3 for Mg-Zn/10TCP, and 1.86 g/cm^3 for Mg-Zn/15TCP).

The cross-sections of the as-sintered porous Mg-Zn/TCP struts were observed using SEM and the elemental compositions were detected or mapped using a SEM equipped with X-ray energy dispersive spectroscopy (EDS, JEOL JSM-IT100, Japan). A counting area size of 81.9 μm by 65.0 μm , a counting time of 15 min, a live-time correction of 3% on average, and an acceleration voltage of 15 kV were used for EDS mapping. The porosities and the phase fractions in the struts were measured from the SEM images using ImageJ. The distribution of the β -TCP particles in the Mg-Zn/TCP composites was quantified by the β value that was obtained from the quadrat method described above.

The phases in the Mg-Zn/TCP composite scaffolds were identified using an X-ray diffractometer (XRD, D8 Advance, Bruker, USA) equipped with a graphite monochromator and a Lynxeye position-sensitive detector. A scan range of 20–100 $^{\circ}$ and a step size of 0.030 $^{\circ}$ using Co $K\alpha$ radiation were employed.

Nanoindentation tests were conducted on a polished Mg-Zn/5TCP specimen using a Nano indenter (G200, KLA, California) equipped with a standard Berkovich tip. A total number of 400 indentations were performed on the struts of the scaffolds with a minimum distance of 40 μm between every two indentations. The indented specimens were then examined with SEM.

The surface roughness of the scaffolds was measured using a digital optical microscope (Keyence, VH-6000). The function of “Roughness” was used and the linear average surface roughness (R_a) was acquired. Roughness values of three struts on each sample were measured.

2.4. In vitro immersion tests

The *in vitro* immersion tests of the Mg-Zn/5TCP and Mg-Zn/10TCP composite scaffolds were performed using a revised simulated body fluid (r-SBF) [45] for up to 28 d. Since the Mg-Zn/15TCP composite scaffolds collapsed after 8 d of immersion, the results are displayed only until day 7. The test conditions were as follows: immersion for 1, 3, 7, 14, and 28 d; temperature = 37 ± 0.5 $^{\circ}C$; pH (r-SBF) = 7.40; 7 mL medium per 1 cm^2 of the scaffold surface area. During the *in vitro* degradation tests, the pH values of the media were recorded using a pH electrode (InlabNMR, METTLER TOLEDO).

To determine the *in vitro* corrosion rates of the composite scaffolds, X-ray micro-computed tomography (μ CT, Nanotom 180 NF, GE Phoenix) with a resolution of 6 μ m was used to scan the composite scaffolds before and after *in vitro* degradation. The obtained μ CT images were reconstructed and exported into Dragonfly (Object Research Systems, Canada). After segmenting the corrosion products from the degraded composite scaffolds in the Dragonfly software, the volumes of the Mg-Zn/TCP composite scaffolds before and after degradation were calculated by using the function “bone analysis”. The volume loss and the corresponded average corrosion rate were determined as:

$$\text{Volume loss [\%]} = \frac{(V_{Mg \text{ before degradation}} - V_{Mg \text{ after degradation}})}{V_{Mg \text{ before degradation}}} \times 100\% \quad (4)$$

$$\text{Corrosion rate [mm/y]} = 8.76 \times 10^4 \times \frac{V}{A \times t} \quad (5)$$

where $V_{Mg \text{ before degradation}}$ and $V_{Mg \text{ after degradation}}$ are the volumes of the composite scaffold before immersion and after immersion [cm^3], respectively, V is the loss of volume [cm^3] (i.e., $V_{Mg \text{ before degradation}} - V_{Mg \text{ after degradation}}$), A is the surface area of the composite scaffold [cm^2], and t is the duration of *in vitro* immersion [h].

By incorporating the corrosion products into Dragonfly, the volumes and porosities of the Mg-Zn/TCP composite scaffolds after immersion for different durations were calculated using the “bone analysis” function.

2.5. Characterization of the biodegradation products

Following uninterrupted immersion until the selected time points (i.e., 1, 3, 7, 14, and 28 d), the morphological characteristics of the biodegradation products on the periphery and at the center of the Mg-Zn/TCP composite scaffolds were observed under SEM (JEOL JSM-IT100, Japan). The chemical elements present in the degradation products and their compositions were analyzed using EDS, while the phase identification was carried out by using XRD (Bruker D8 Advance diffractometer in the Bragg-Brentano geometry).

From the CT images of Mg-Zn/5TCP, Mg-Zn/10TCP and Mg-Zn/15TCP composite scaffold samples, the peripheral (the 100th slice from the top) and central slices (the 500th slice from the top) were selected to reveal the deposition of the corrosion products inside the composite scaffolds.

2.6. Uniaxial compression tests

The compressive mechanical properties of the Mg-Zn/TCP composite scaffolds, as well as the specimens retrieved at the selected time points of the *in vitro* immersion tests, were determined using a mechanical testing machine (Zwick Z100, Germany) with a 10 kN load cell. The tests were performed using a crosshead speed of 2 mm/min. The quasi-elastic gradient (hereafter referred to as Young's modulus), yield strengths and compressive stress of the specimens were determined according to ISO 13314: 2011. The slope of the initial linear line in the stress-strain curve was taken as the Young's modulus. A 0.2% offset line, parallel to the linear region, was defined and the intersection with the curve was taken as the yield strength. Compressive stress was determined by the first local maximum stress in the stress-strain curve.

2.7. Cytocompatibility of the composite scaffolds

2.7.1. Cell culture

Mouse preosteoblast cells (MC3T3-E1, Sigma Aldrich, Germany) were pre-cultured for 7 d in α -minimum essential medium (α -MEM, Thermo Fisher Scientific, USA), supplemented with 10% fetal bovine serum (FBS, Thermo Fisher Scientific, USA) and 1% penicillin/streptomycin (p/s, Thermo Fisher Scientific, USA). The medium was refreshed every 2–3 d

2.7.2. Cell viability and cell adhesion

Prior to cell seeding, the scaffolds were sterilized by heating to 120 °C for 2 h. The samples were incubated for 3 days with the α -minimum essential medium (α -MEM). The MC3T3-E1 preosteoblasts (1×10^4 cells per sample) were seeded onto the Mg-Zn/TCP specimens (2.4 mm in height and 9.25 mm in diameter) in 8 mL α -MEM (without ascorbic acid, but with 10% FBS, 1% p/s) in 6-well plates. The porous Mg-Zn scaffolds were used as the control group. The viability of the preosteoblasts was examined using a live/dead assay (LIVE/DEAD Viability/Cytotoxicity Kit, Life Technologies Corp., USA) in duplicate. After 3 d of cell culture, the specimens with the cells were stained using calcein and ethidium homodimer-1 (Thermo Fisher Scientific, USA). Thereafter, the live and dead cells on the scaffolds were observed with a fluorescence microscope (ZOE cell imager, Bio-Rad, USA). In addition, the trypan blue assay (Bio-Rad, USA) was used for the quantification of cell viability on the scaffolds in triplicate. For each group, the scaffolds without cells were used as the background control. After 1, 3, 7 and 14 d of cell culture, the cells were trypsinized from the specimens and the well plates. After centrifuging, the cell suspensions were obtained. 10 μ L of trypan blue dye was used to mix with 10 μ L of each cell suspension which was subsequently pipetted into a dual-chamber cell counting slide. The living cells were counted using an automated cell counter (TC20, Bio-Rad, USA). After subtracting the number obtained from the background control, the mean and standard deviation of the number of the living cells of each group were obtained. To examine the cell adhesion and morphology on the scaffolds, the specimens were fixed and dehydrated, after the preosteoblasts were cultured on them for 3 d. Then, the specimens were sputtered with gold and were observed by SEM.

2.7.3. Osteogenic response

To evaluate the bioactivity of the developed composites, the extracts of the Mg-Zn/TCP composite scaffolds were prepared through immersing the sterilized composite scaffolds in α -MEM under the above physiological conditions for 72 h. The extracts were supplemented with ascorbic acid and β -glycerophosphate. For both ALP test and Alizarin Red S, the supplementary medium only was used as control group. Both the ALP test and Alizarin Red S test were performed in triplicate for each group. An alkaline phosphate (ALP) activity test was performed after 14 d of cell culture in the extracts using an alkaline phosphatase assay kit (ab83371, Abcam, USA). For the ALP tests, the culture medium was supplemented with 50 μ g mL^{-1} ascorbic acid (1:1000) and 4 mM β -glycerophosphate (1:500) (both from Sigma Aldrich, Germany). The ALP test process followed the product manufacturer's protocol (ab83371, Abcam, USA).

In addition, Alizarin Red S staining was performed after 21 days to assess calcium in the matrix of cells. The cells were cultured in the prepared extracts supplemented with ascorbic acid and β -glycerophosphate, as described above. After 21 d of cell culture, the specimens were fixed using a 4% (v/v) formaldehyde solution (Sigma Aldrich, Germany). The specimens were then incubated in a 2% (w/v) Alizarin Red S solution (Sigma Aldrich, Germany) for 30 min in the dark. The specimens were then rinsed five times

Table 1

The recovery degrees (R) of the inks as determined by the creep-recovery tests ($n = 3$ per group; for R calculation, shear stress was applied for 60 s and the remained strain was measured for 180 s).

Sample group	97% pre-inks	95% pre-inks	93% pre-inks
Mg-Zn/5TCP	26% ± 12%	–	–
Mg-Zn/10TCP	–6% ± 5%	19% ± 2%	–
Mg-Zn/15TCP	–1% ± 1%	9% ± 3%	29% ± 8%

with distilled water before being imaged by a ZOE fluorescent cell imager (Bio-Rad, The Netherlands). The quantification was performed by exposing the stained specimens to a solution of 20% methanol and 10% acetic acid. After 15 min, the absorbance of Alizarin Red was read on a Victor X3 plate reader (Perkin Elmer, The Netherlands) at a wavelength of 450 nm.

2.8. Statistical analysis

The results of the viable cell count, ALP activity, and Alizarin Red S absorption tests were statistically analyzed using two-way ANOVA, followed by a Tukey multiple comparison *post hoc* test (**** = $p < 0.0001$, *** = $p < 0.001$, ** = $p < 0.01$, and * = $p < 0.05$, *n.s.* = not significant). The SPSS Statistics 20 software (IBM, USA) was used for the statistical analysis.

3. Results

3.1. Ink characteristics

The dispersions of β -TCP particles in the binder with the β -TCP/binder volume ratios of 7:93, 5:95, and 3:97 are shown in Fig. 2A-(a-c), respectively. Some agglomerates of β -TCP particles were clearly visible in the 93% pre-ink group (Fig. 2A-a), while in the 95% (Fig. 2A-b) and 97% pre-ink groups (Fig. 2A-c), the dispersions of β -TCP particles were more uniform. The β value, indicating the degree of inhomogeneity, was 1.2 ± 0.2 for the 93% pre-ink group, 0.6 ± 0.3 for the 95% pre-ink group, and 0.4 ± 0.2 for the 97% pre-ink group.

The Mg-Zn powder particles were further mixed with the pre-inks (*i.e.*, the mixtures of the binder and β -TCP) to prepare the inks for 3D printing. The dispersions of the β -TCP particles in the printed specimens (Mg-Zn/10TCP as an example here) exhibited the same trend (Fig. 2A-(d-f)) as for the pre-inks. Large clusters of β -TCP particles were still visible in the specimens that were 3D printed using the 93% pre-ink (Fig. 2A-d), which sometimes even resulted in clogging the nozzle during 3D printing (Fig. S1a). The β -TCP particles were most uniformly distributed on the surfaces of Mg-Zn powder particles, when using the 97% pre-ink for 3D printing, with more binder covering the powder particles (Fig. 2A-f).

The 97% pre-ink allowed a highly uniform distribution of the β -TCP particles in the printed specimens. Therefore, it was first used for preparing the Mg-Zn/5TCP, Mg-Zn/10TCP, and Mg-Zn/15TCP inks to check their printability. All the three groups of the prepared inks using the 97% pre-ink exhibited shear-thinning (Fig. 2B-a and b, denoted as Mg-Zn/5TCP_97%, Mg-Zn/10TCP_97% and Mg-Zn/15TCP_97%, respectively). However, the Mg-Zn/10TCP_97% and Mg-Zn/15TCP_97% inks did not show quick recovery when the applied shear stress was removed (Fig. 2A-c and d), with recovery degrees of –6% and –1%, respectively (Table 1). These two inks were, thus, not suitable for the extrusion-based 3D printing [28]. This was further evidenced by the non-freeform characteristics of the specimens printed with the Mg-Zn/10TCP_97% or Mg-Zn/15TCP_97% (Fig. 2C-a). The 95% pre-ink was, therefore, used to prepare the Mg-Zn/10TCP and Mg-Zn/15TCP inks (denoted as Mg-Zn/10TCP_95% and Mg-Zn/15TCP_95%, respectively). Similar to the

Mg-Zn/5TCP_97% ink, the Mg-Zn/10TCP_95% ink exhibited shear-thinning (Fig. 2B-a) while the deformation did recover when the applied stress was removed (Fig. 2B-c), which allowed for the realization of freestanding 3D structures without any deflection of the spanning struts (Fig. 2C-c). The Mg-Zn/15TCP_95% inks showed a much lower recovery degree, as compared to the printable inks (Table 1) and the resulting structure showed a large degree of the deflection of the strut layer (Fig. 2C-b). Eventually, the Mg-Zn/15TCP_93% ink (prepared using 93% pre-ink) with a recovery degree of 29% was chosen as it enabled the successful printing of Mg-Zn/15TCP 3D structures. Based on the above rheological results and the quality of the resulting composite scaffolds, the 97% pre-ink was chosen for printing the Mg-Zn/5TCP composite scaffolds, while the 95% and 93% pre-inks were used for printing the Mg-Zn/10TCP and Mg-Zn/15TCP composite scaffolds, respectively.

3.2. Characteristics of the porous Mg-Zn/TCP composite scaffolds

Using the optimally formulated inks, the Mg-Zn/5TCP, Mg-Zn/10TCP, and Mg-Zn/15TCP composite scaffolds could be successfully printed. All the three groups of the printed Mg-Zn/TCP composite scaffolds showed a geometrically ordered porous structure with a $0^\circ/90^\circ/0^\circ$ pattern (Fig. S2-(a-c)), as designed. The struts aligned accurately without any deflection over the spanning space and the adjacent layers adhered to each other (Fig. S2a-c). From the close-up views of the struts in the composite scaffolds, the β -TCP particles and the binder uniformly covered the Mg-Zn powder particles in the Mg-Zn/5TCP (Fig. S2-d) and Mg-Zn/10TCP scaffolds (Fig. 2A-e). However, the β -TCP particles agglomerated on the surfaces of Mg-Zn powder particles in the Mg-Zn/15TCP specimens (Fig. S2-e).

After sintering, the porosities of the struts were $0.1 \pm 0.11\%$ for Mg-Zn/5TCP, $0.3 \pm 0.23\%$ for Mg-Zn/10TCP, and $13.9 \pm 4.7\%$ for Mg-Zn/15TCP. The other detailed structural characteristics of the composite scaffolds are presented in Table 2. The as-sintered Mg-Zn/5TCP and Mg-Zn/10TCP composite scaffolds showed highly densified struts with almost no apparent pores (Fig. 3A-a1 and b1), while the Mg-Zn/15TCP composite scaffolds had porous struts (Fig. 3A-c1). The edges of the original Mg-Zn powder particles disappeared due to liquid-phase sintering. The Mg-Zn alloy matrix with dispersed β -TCP particles was observed on the surfaces of all the three groups of the Mg-Zn/TCP composite scaffolds (Fig. 3A-(a2-c2)). The cross-sectional images of the Mg-Zn/5TCP and Mg-Zn/10TCP composite scaffolds revealed almost uniform distributions of the bioceramic phase (Fig. 3A-a3 and b3), while clustering was predominately observed in the Mg-Zn/15TCP composite scaffolds (Fig. 3A-c3). The degrees of the inhomogeneity of the bioceramic phase in the three groups of the composite scaffolds were quantified (Table 4). The Mg-Zn/15TCP group had a higher β value than the Mg-Zn/5TCP and Mg-Zn/10TCP groups, confirming the presence of more agglomerates in the Mg-Zn/15TCP composite scaffolds.

In addition to the Mg-Zn matrix phase, another two phases, namely an integrated gray phase (arrow 1 in Fig. 3A-a4 and b4) and an isolated particle-shaped phase (arrow 2 in Fig. 3A-b4), were present in all the three Mg-Zn/TCP composite scaffold groups, as shown in the amplified cross-sectional images (Fig. 3A-(a4-c4)). XRD revealed that besides the Mg-Zn matrix phase and the MgO phase, inevitably present in the Mg samples due to the sintering process, there were two new phases, *i.e.*, the $\text{Ca}_2\text{Mg}_6\text{Zn}_3$ and $\text{Ca}_4\text{P}_2\text{O}$ phases, but no β -TCP phase was detected (Fig. 3B), indicating that diffusion between the Mg-Zn matrix and β -TCP occurred during sintering.

To identify the two new phases in the composite scaffolds, EDS mapping was used to examine the elemental compositions. The integrated gray phase was found to be mainly composed of Ca,

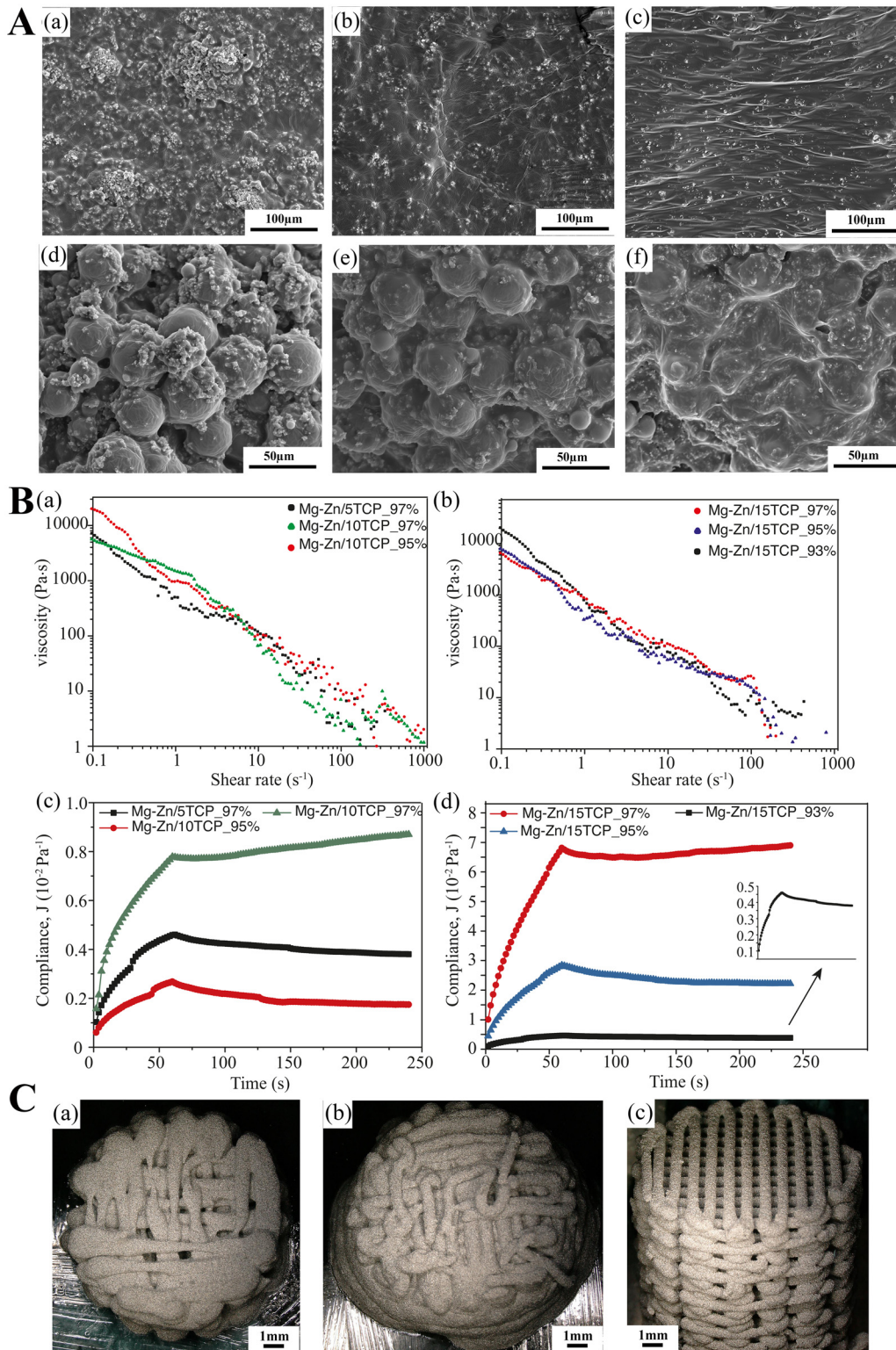


Fig. 2. (A) The dispersion of β -TCP particles in the 93% pre-ink (a), 95% pre-ink (b), and 97% pre-ink (c) (SEM, JEOL, $\times 250$), and the distribution of the β -TCP particles in the Mg-Zn/10TCP specimens printed using the 93% pre-ink (d), 95% pre-ink (e), and 97% pre-ink (f), (SEM, JEOL, $\times 500$) (B) the rheological characteristics of the prepared inks: results obtained from the shear rate sweep tests (a)-(b) and the results obtained from the creep-recovery tests (c)-(d); (C) the macrographs of representative samples printed using the prepared inks (optical microscope, Keyence, $\times 50$): Mg-Zn/15TCP_97% or Mg-Zn/10TCP_97% inks (a), Mg-Zn/15TCP_95% ink (b), and Mg-Zn/5TCP_97%, Mg-Zn/10TCP_95%, or Mg-Zn/15TCP_93% (c).

Table 2

The morphological characteristics of the extrusion-based 3D printed Mg-Zn/ β -TCP composite scaffolds ($n = 3$; an optical microscope was used for measuring strut width and spacing, as well as the porosity of the struts; the weighing method was used for the measurement of absolute porosity).

Sample group	Strut width (μm)	Strut spacing (μm)	Porosity in the struts after sintering	Absolute porosity of the scaffolds
Design	580	360	–	37.8%
Mg-Zn	516.1 \pm 15.3	331.7 \pm 39.5	6.9 \pm 1.0%	50.3 \pm 3.4%
Mg-Zn/5TCP	456.3 \pm 13.9	310.8 \pm 18.8	0.1 \pm 0.1%	47.6 \pm 10.6%
Mg-Zn/10TCP	429.2 \pm 17.6	316.6 \pm 23.0	0.3 \pm 0.2%	48.5 \pm 4.0%
Mg-Zn/15TCP	451.7 \pm 14.8	362.3 \pm 27.2	13.9 \pm 4.7%	55.2 \pm 17.9%

Table 3

The EDS point analysis of the Mg-Zn/ β -TCP specimens shown in Fig. 4B.

Weight%	C	O	Mg	P	Ca	Zn
#1	2.5	6.4	52.2	0.4	10.8	27.7
#2	2.4	3.2	47.7	0.5	13.6	32.5
#3	4.7	12.6	55.7	1.2	12.7	13.1
#4	5.1	17.6	50.0	1.2	12.9	13.3

Table 4

The β values, indicating the distribution degree of bioceramic particles, and the volume fractions of the new phases in the Mg-Zn/ β -TCP specimens ($n = 3$ per group; the quadrat method was applied to the SEM images for the calculation of the β values; ImageJ was used for the estimation of the phase fractions).

Sample group	β	Ca ₄ P ₂ O	Ca ₂ Mg ₆ Zn ₃
Mg-Zn/5TCP	0.51 \pm 0.1	0.20% \pm 0.10%	6.70% \pm 1.32%
MgZn/10TCP	0.63 \pm 0.2	0.93% \pm 0.51%	10.07% \pm 2.50%
MgZn/15TCP	1.52 \pm 0.2	2.39% \pm 1.16%	15.32% \pm 2.97%

Zn and Mg, which suggests the presence of Ca₂Mg₆Zn₃ (Fig. 4A). The isolated particle-shaped phase was mostly attached to the integrated gray phase, which could be readily observed in the scaffolds with higher β -TCP concentrations (i.e., Mg-Zn/10TCP and Mg-Zn/15TCP, Fig. 4B, and Fig. S3). EDS mapping could, therefore, not distinguish these two phases. EDS point analysis was consequently used to identify each phase. Compared with points 1 and 2, points 3 and 4 had more O and P but less Zn (Fig. 4B and Table 3). Combined with the XRD results, the isolated particles could be identified as Ca₄P₂O. The volume fractions of Ca₂Mg₆Zn₃ and Ca₄P₂O in the composite scaffolds are listed in Table 4.

The nanohardness of the Mg-Zn matrix was 43.0 \pm 3.0 GPa, while that of the Ca₂Mg₆Zn₃ and Ca₄P₂O phase combination was 55.1 \pm 8.0 GPa (Fig. 4C and D). In addition, the surface roughness values of Mg-Zn/5TCP, Mg-Zn/10TCP, and Mg-Zn/15TCP, *R_a*, were 5.9 \pm 1.5 μm , 8.8 \pm 5.6 μm , and 9.1 \pm 1.2 μm , respectively.

3.3. In vitro degradation performance of the composite scaffolds

During the *in vitro* immersion tests in r-SBF, white corrosion products gradually deposited on the composite scaffolds (Fig. 5a, Fig. S4a, and Fig. S5a). The biodegradation behavior of both the peripheral and central layers in the composite scaffolds could be observed on the 2D slices of the μCT reconstructions (Fig. 5a, Fig. S4a, and Fig. S5a). The struts (white part) on the periphery and at the center of the composite scaffolds gradually biodegraded and were replaced by the biodegradation products (gray part). The struts at the central layers degraded more than those on the periphery for all the three Mg-Zn/TCP groups (Fig. 5a, Fig. S4a, and Fig. S5a). During the *in vitro* biodegradation, the biodegradation products stayed in the composite scaffolds. With increasing immersion time, more and more biodegradation products replaced the struts and occupied the spaces between the struts (i.e., filling in the macropores of the composite scaffolds, Fig. 5a, Fig. S4a, and Fig. S5a). The degradation products entrapped in the composite scaffolds in-

creased the volumes of the composite scaffolds at the beginning of the *in vitro* immersion, when the degradation products were included during the segmentation of the composite scaffolds (Fig. 5b, Fig. S4b, and Fig. S5b). The relative densities of the Mg-Zn/5TCP and Mg-Zn/10TCP composite scaffolds also showed an increasing trend (corresponding to the decreasing porosities of the composite scaffolds) until day 14 (Fig. 5c, Fig. S4c). However, when the biodegradation products were segmented apart from the scaffold substrates, the volumes and relative densities showed a decreasing trend with immersion time for all the three Mg-Zn/TCP groups (Fig. 5b and c, Fig. S4b and c, and Fig. S5b and c). At the beginning of the *in vitro* immersion, the *in vitro* biodegradation rates of the scaffolds were 1.0 \pm 0.4 mm/y for Mg-Zn/5TCP, 1.6 \pm 0.7 mm/y for Mg-Zn/10TCP, and 4.1 \pm 3.4 mm/y for Mg-Zn/15TCP, respectively (Fig. 5d). After 28 days, the biodegradation rates of Mg-Zn/5TCP and Mg-Zn/10TCP decreased to 0.5 mm/y and 0.7 mm/y, respectively. The biodegradation rate of Mg-Zn/15TCP decreased to 2.3 \pm 0.4 mm/y after 7 d of immersion (Fig. 5d). During the *in vitro* degradation, Mg ions were gradually released into r-SBF. Mg-Zn/15TCP released Mg ions the most at day 7 (Fig. 5e) and had the highest pH level (Fig. S6), which is consistent with this high rate.

3.4. Characteristics of the biodegradation products

A layer of biodegradation products formed and covered the struts of the Mg-Zn/10TCP specimens after 24 h of immersion (Fig. 6a). The biodegradation products grew with the immersion time and almost filled the spaces (i.e., macropores) between the struts after day 14 (Fig. 6b-c). The Mg-Zn/5TCP specimens showed a similar biodegradation behavior (Fig. S7a-c). As for the Mg-Zn/15TCP specimens, the degradation of the struts was noticeable only after 3 d of immersion and the formed biodegradation products showed a rather bumpy morphology (Fig. S8b-c). The magnified images of biodegraded Mg-Zn/10TCP showed the appearance of riverbed-like biodegradation products (Fig. 6d) which were followed by the gradual formation of cauliflower-like biodegradation products that almost fully covered the surface at day 14 (Fig. 6e-f). The major elements present in the peripheral biodegradation products were C, O, Mg, Ca, and Zn. Similar observations were made for the Mg-Zn/5TCP and Mg-Zn/15TCP specimens (Fig. S7 and Fig. S8). At the center of the specimens, the biodegradation products contained MgO, replacing the original struts as biodegradation progressed (gray area), while CaP-containing compounds (white area) became deposited between the struts (Fig. 6g, Fig. S7g, Fig. S8g, and the corresponding EDS mappings).

In addition, XRD was used to examine the phases in the biodegraded scaffolds. In addition to the Mg matrix phase, Ca₂Mg₆Zn₃, and Ca₄P₂O that were present in the as-sintered scaffolds, the following phases were identified in the biodegraded Mg-Zn/TCP specimens: MgO, Mg(OH)₂, ZnO, brushite (CaHPO₄·2H₂O), and CaCO₃·H₂O (Fig. 7 and Fig. S9). The intensities of the Mg peaks clearly decreased with the immersion time (lines 1 in Fig. 7 and Fig. S9) while the peaks corresponding to Mg(OH)₂ intensified (lines 2 in Fig. 7 and Fig. S9). The brushite peaks disappeared after 14 d of immersion (lines 3 in Fig. 7).

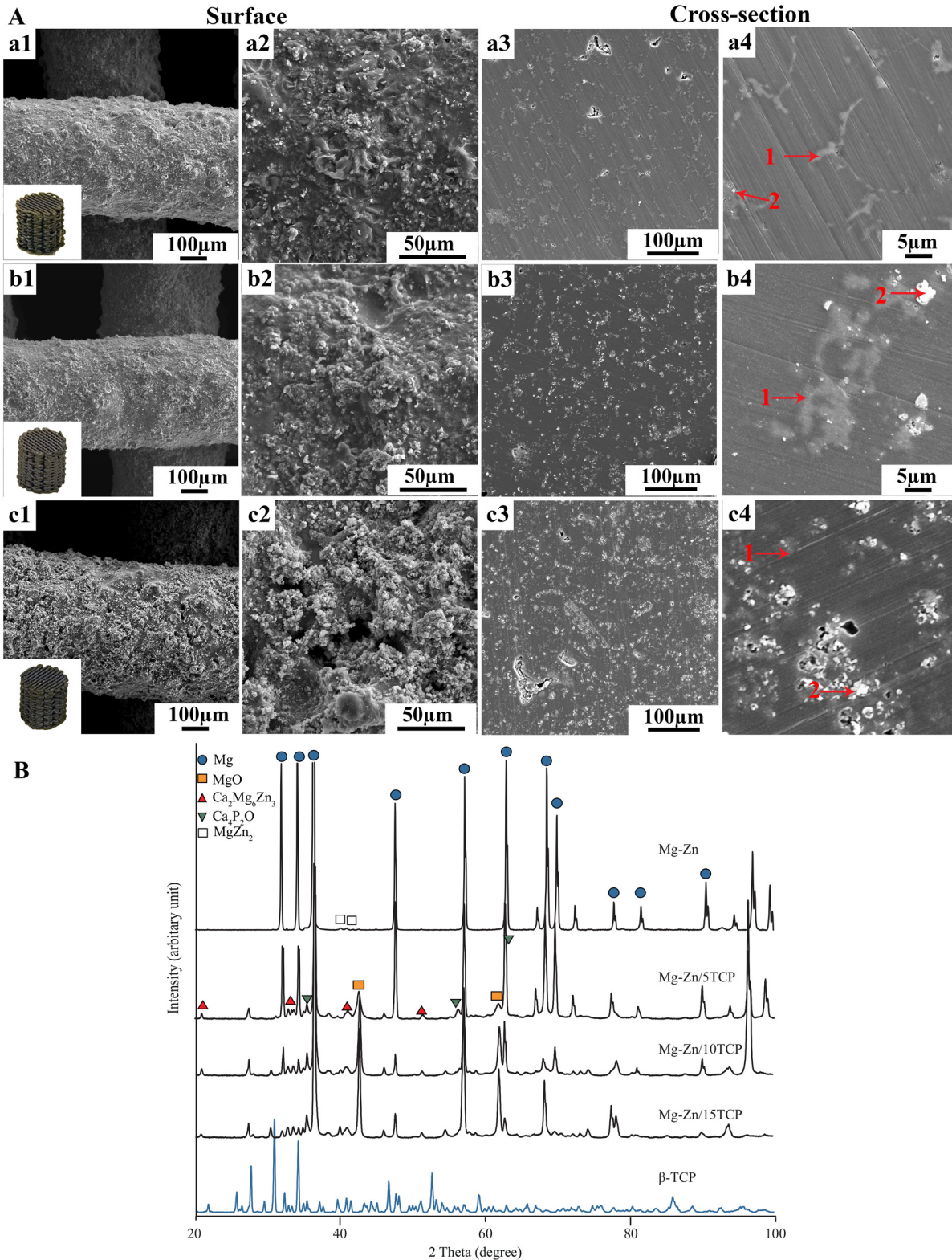


Fig. 3. The characteristics of the fabricated Mg-Zn/TCP composite scaffolds (SEM, JEOL): (A) microstructures: (a1-a4) Mg-Zn/5TCP, (b1-b4) Mg-Zn/10TCP, (c1-c4) Mg-Zn/15TCP; (B) XRD patterns (Bruker, ICDD card number: Mg, 04-019-3684; MgO, 04-010-4039; $\text{Ca}_2\text{Mg}_6\text{Zn}_3$, 00-012-0266; $\text{Ca}_4\text{P}_2\text{O}$, 04-010-2306; β -TCP, 00-055-0898).

3.5. Mechanical properties along with in vitro degradation

Under uniaxial compression, all the Mg-Zn/TCP composite scaffolds exhibited smooth stress-strain curves that started with a linear elastic region, followed by a plastic deformation region

(Fig. 8a). The yield strengths of the as-sintered composite scaffolds were 24.4 ± 13.4 MPa for Mg-Zn/5TCP, 31.3 ± 1.9 MPa for Mg-Zn/10TCP, and 23.5 ± 0.6 MPa for Mg-Zn/15TCP. The elastic moduli of the three groups of the as-sintered composite scaffolds were 431.6 ± 102.9 MPa, 585.3 ± 117.6 MPa, and 455.7 ± 53.7 MPa,

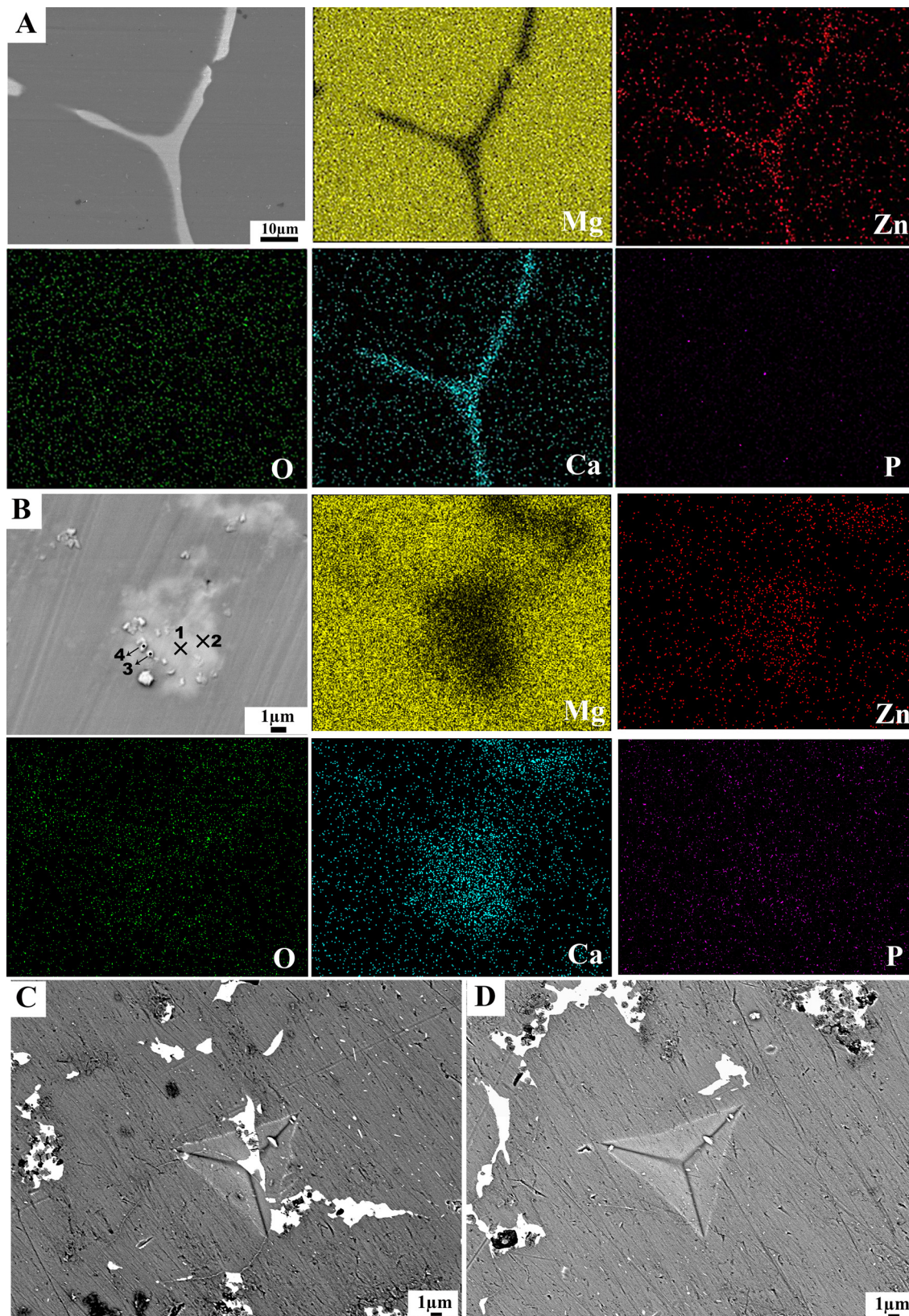


Fig. 4. The characteristics of the phases in the Mg-Zn/TCP composite scaffolds (SEM, JEOL, $\times 1500$): (A) the phases in Mg-Zn/5TCP and the corresponding EDS mapping, (B) the phases in Mg-Zn/10TCP and the corresponding EDS mapping, (C) nano-indentation (G200, Berkovich tip, maximum indentation depth of 2000 nm) on the $\text{Ca}_2\text{Mg}_6\text{Zn}_3$ and $\text{Ca}_4\text{P}_2\text{O}$ combined phases, and (D) nano-indentation on the Mg-Zn matrix.

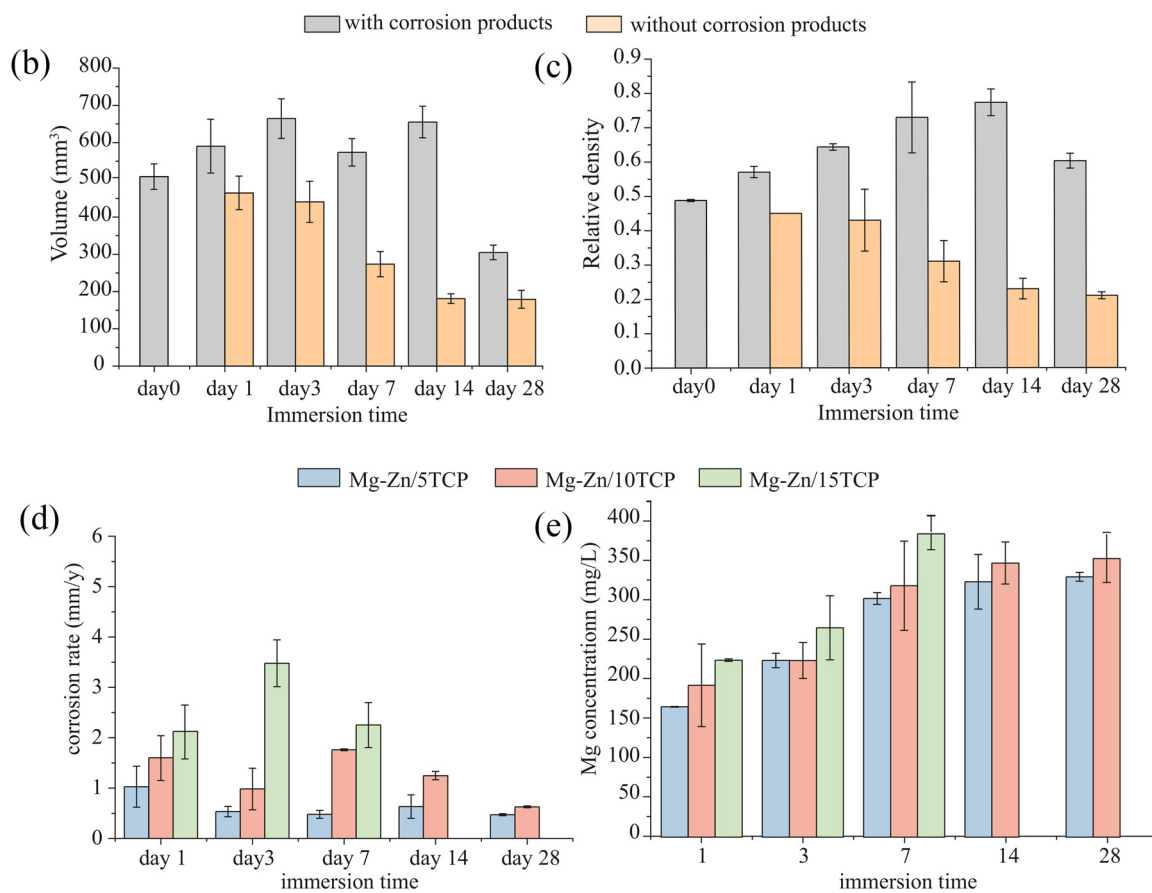
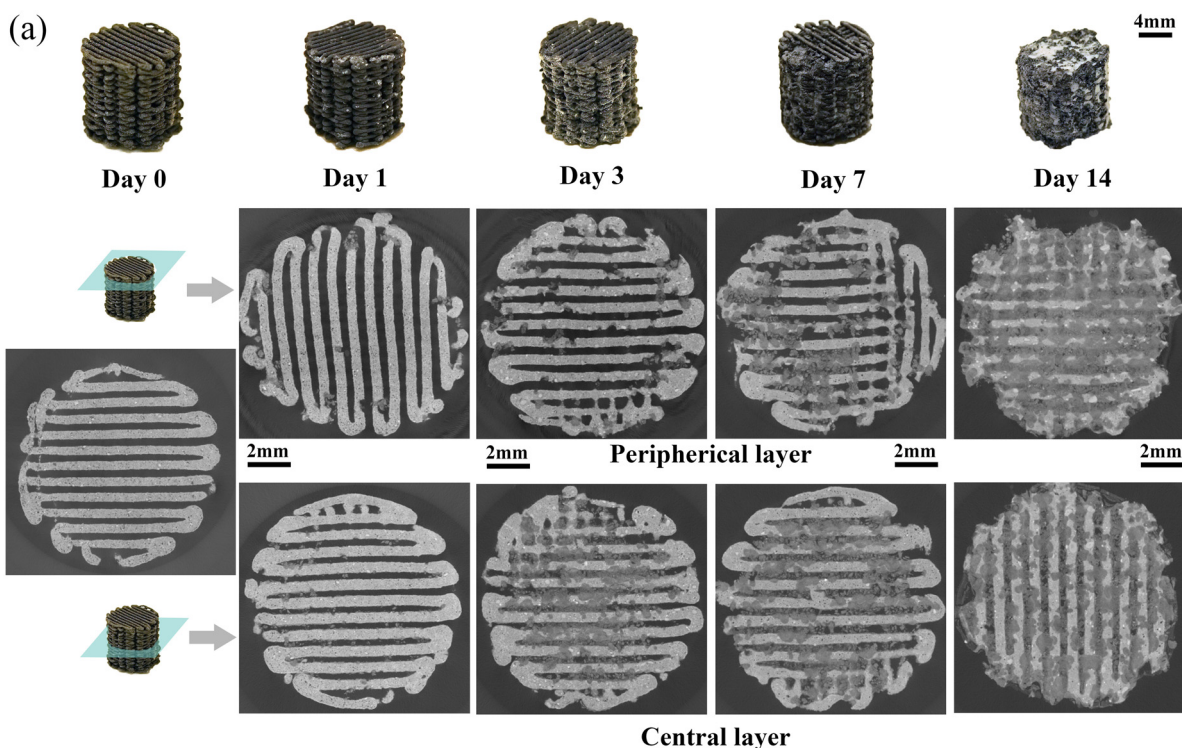


Fig. 5. *In vitro* degradation behavior: (a) the macrographs and 2D μ CT slices of the degraded Mg-Zn/10TCP specimens, (b-c) the changes in the volumes and relative densities of the degraded Mg-Zn/10TCP specimens with and without corrosion products, (d) corrosion rates, and (e) changes of Mg ion concentrations in r-SBF up to 28 days.

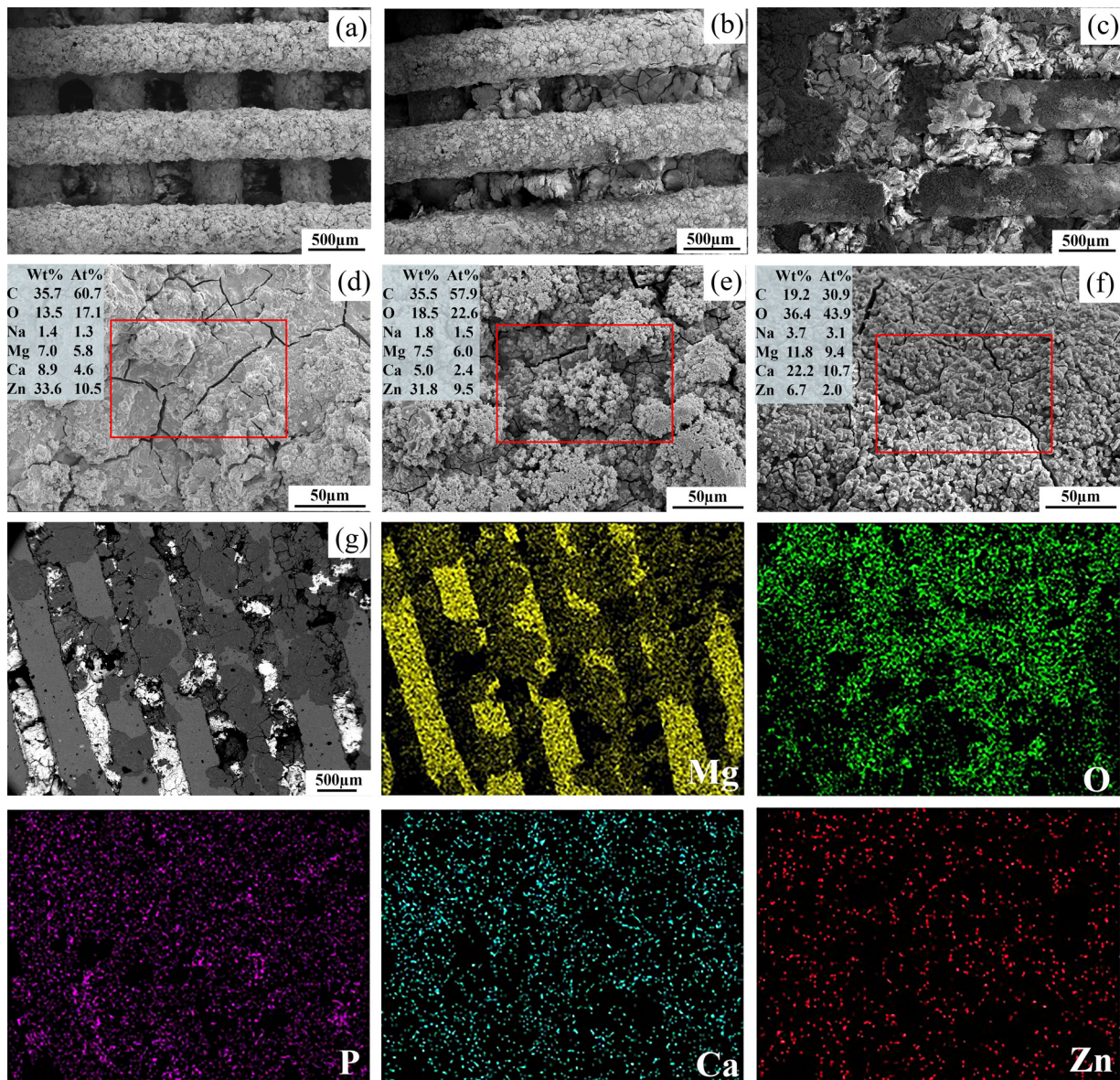


Fig. 6. The morphologies and chemical compositions of *in vitro* biodegradation products on the Mg-Zn/10TCP scaffolds (SEM, JEOL): on the periphery after 1 (a- $\times 40$ and d- $\times 500$), 7 (b- $\times 40$ and e- $\times 500$), 14 days (c- $\times 40$ and f- $\times 500$) of biodegradation, and (g) at the center of the scaffolds after 14 days of biodegradation and the corresponding EDS mapping (acceleration voltage: 15 kV, live-time correction: 3% and counting area: $81.9 \mu\text{m} \times 65.0 \mu\text{m}$). The box areas and values indicate where the EDS analyses were performed and the corresponding elemental compositions, respectively.

respectively. The compressive strengths were 40.9 ± 17.5 MPa for Mg-Zn/5TCP, 39.1 ± 22.7 MPa for Mg-Zn/10TCP, and 29.9 ± 2.5 MPa for Mg-Zn/15TCP. A decline in strain at failure from $19 \pm 7\%$ for Mg-Zn/5TCP to $11 \pm 3\%$ for Mg-Zn/15TCP was observed, indicating that the scaffolds became less ductile with increasing β -TCP percentage. After *in vitro* biodegradation, the yield strengths and elastic moduli of the Mg-Zn/5TCP and Mg-Zn/10TCP specimens remained unchanged or even increased until day 3, followed by a decreasing trend. The mechanical properties of Mg-Zn/15TCP gradually decreased with time throughout the *in vitro* immersion period (Fig. 8b and c).

3.6. In vitro cytocompatibility

High levels of metabolic activity were observed when cells were cultured with the extracts of the Mg-Zn/5TCP and Mg-Zn/10TCP scaffolds (Fig. S10). However, the metabolic activity of the extract of Mg-Zn/15TCP at day 7 was below 20%, indicating its cytotoxic-

ity. Therefore, for direct cell culture assay, only porous Mg-Zn/5TCP and Mg-Zn/10TCP were further tested, with Mg-Zn specimens for comparison purposes. The live/dead staining after 3 d of culture showed homogeneous cell distributions on the struts of all the groups (Fig. 9a-c). Preosteoblasts with a stretching shape were observed on both the Mg-Zn/5TCP (Fig. 9b) and Mg-Zn/10TCP specimens (Fig. 9a). In contrast, the cells on the Mg-Zn scaffolds were mostly red and rounded (Fig. 9c). The SEM imaging confirmed that the cells attached to the Mg-Zn/5TCP and Mg-Zn/10TCP surfaces developed many filopodia and showed spreading morphologies with cell-cell contacts after 3 d of culture (Fig. 9d and e). The viable cells on the Mg-Zn/5TCP and Mg-Zn/10TCP specimens increased until day 7, and their numbers were significantly higher than the number of the cells on the Mg-Zn scaffolds (Fig. 9f). After 14 d of culture, the viable cells on Mg-Zn/5TCP were at the same level as day 7, but those on the Mg-Zn/10TCP specimens decreased.

Both the Mg-Zn/5TCP and Mg-Zn/10TCP specimens showed enhanced levels of ALP activity after 14 d in culture as compared to

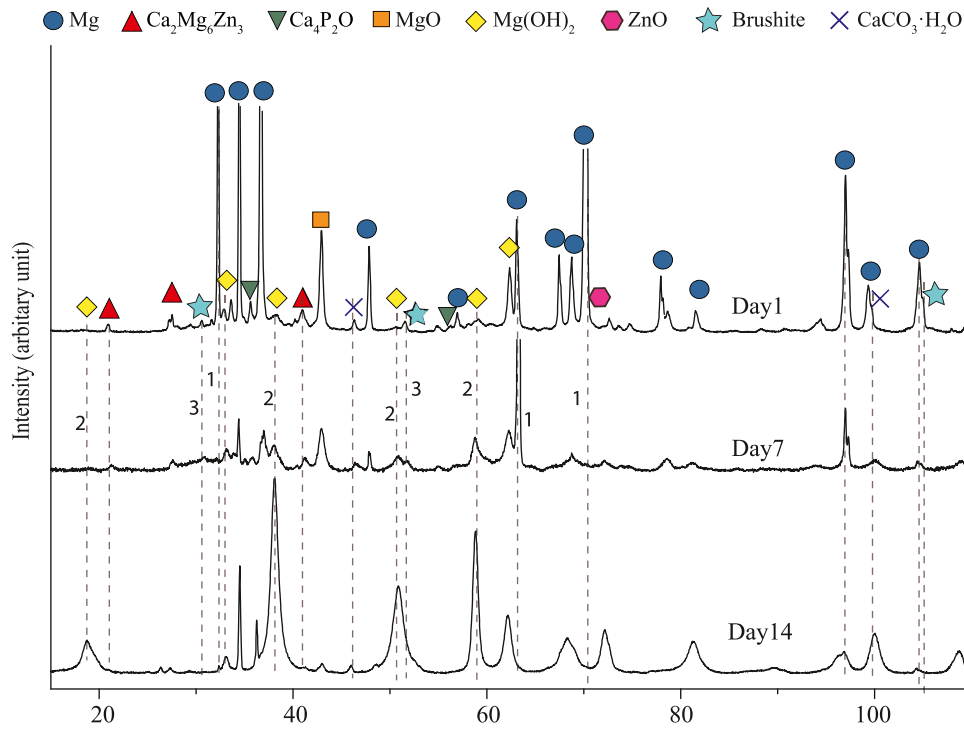


Fig. 7. The XRD (Bruker) patterns of the Mg-Zn/10TCP scaffolds after 1, 7, and 14 days of biodegradation.

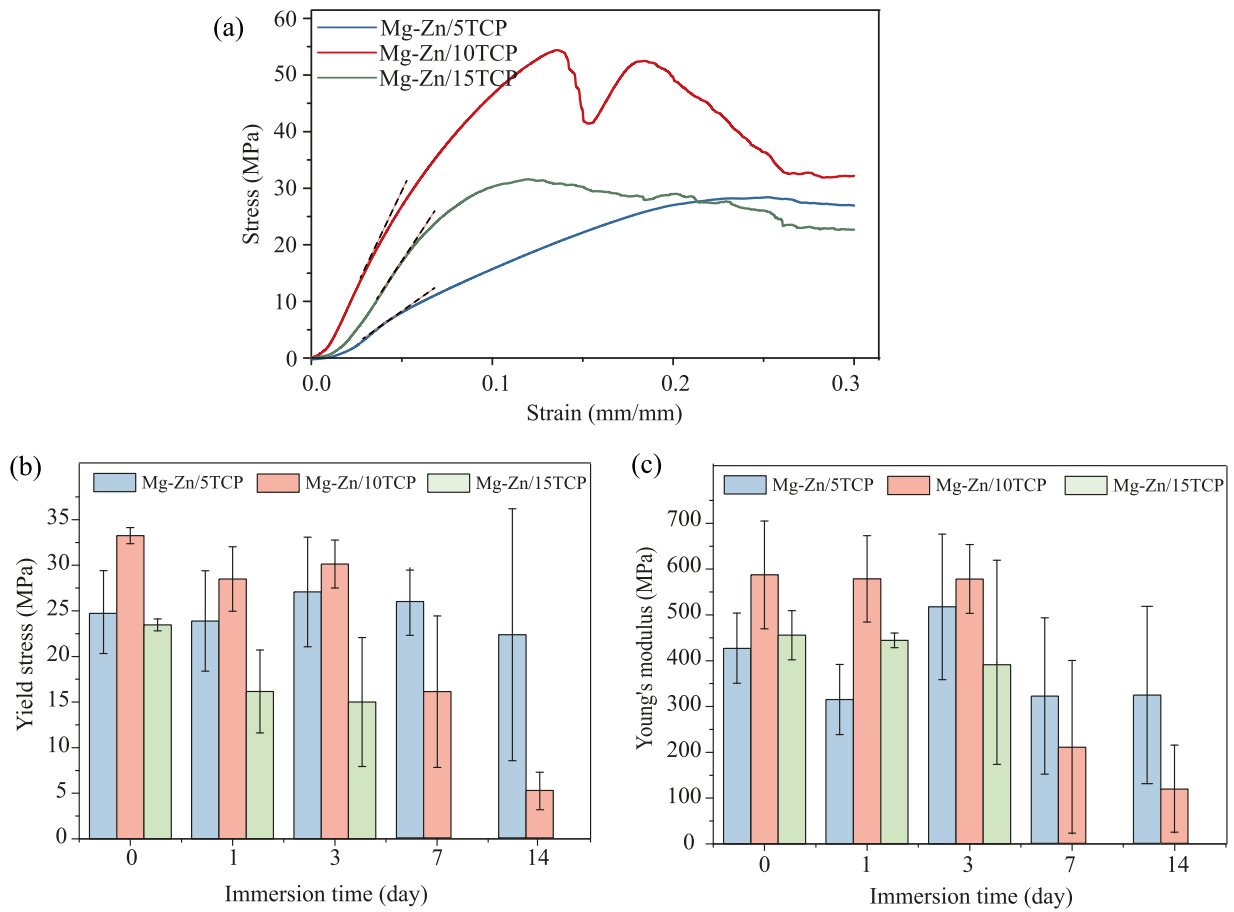


Fig. 8. The compressive properties of the Mg-Zn/10TCP specimens (Zwick, 10 kN load cell, crosshead speed: 2 mm/s): (a) the stress-strain curves of the scaffolds before degradation (the dashed line indicates the linear elastic region), (b) the variations of the yield strength with the immersion time, and (c) the variations of the Young's modulus with the immersion time.

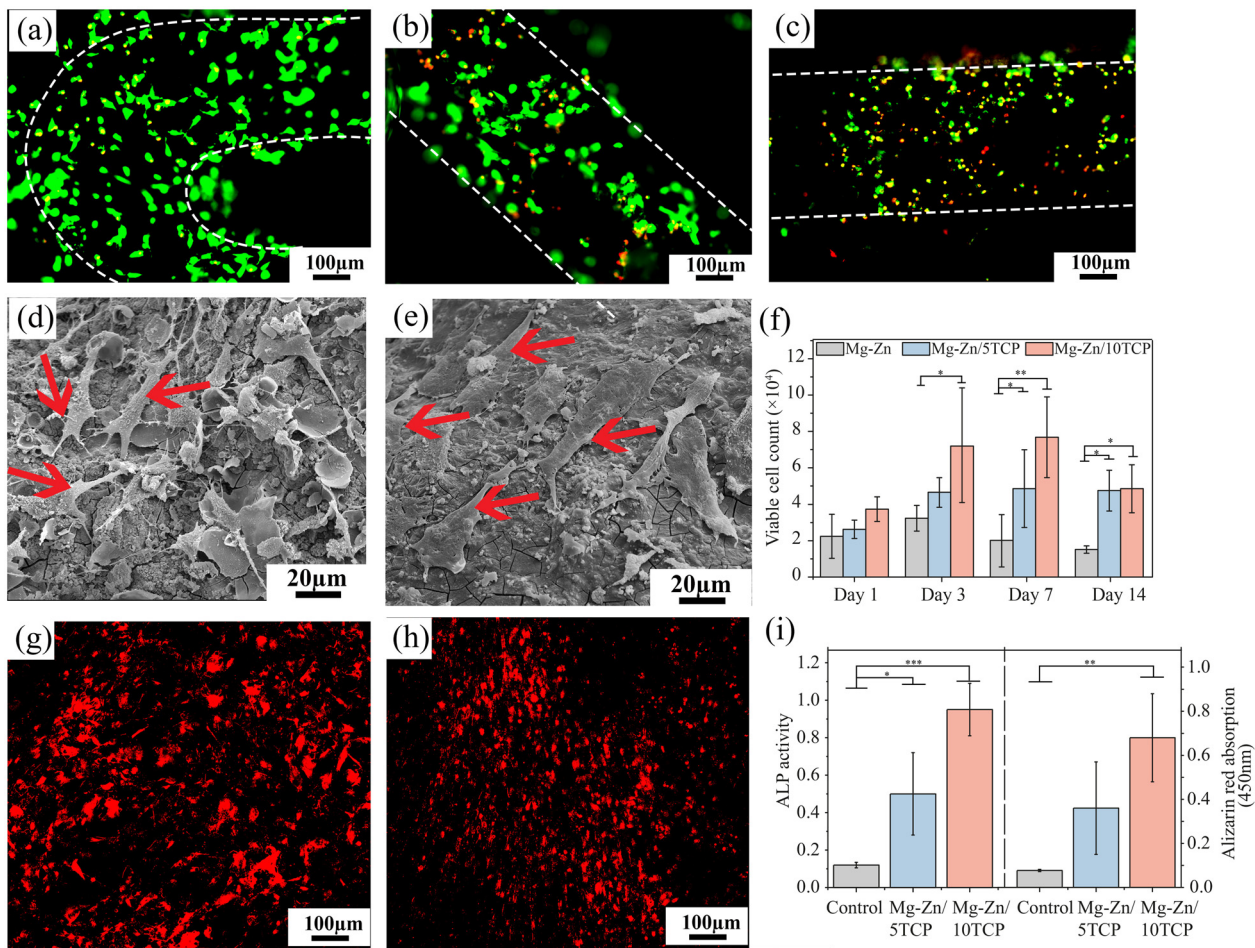


Fig. 9. The *in vitro* biological evaluation of the Mg-Zn/5TCP and Mg-Zn/10TCP specimens: calcein acetoxyethyl (green, showing viable cells) and ethidium homodimer-1 (red, showing damaged cells) fluorescence staining of MC3T3-E1 preosteoblasts after 3 d of culture on Mg-Zn/10TCP (a), Mg-Zn/5TCP (b), and Mg-Zn (c), respectively (the white dashed lines indicate the rough edges of the scaffold struts); the morphologies of the preosteoblasts after 3 d of culture on Mg-Zn/10TCP (d) and Mg-Zn/5TCP (e), and the number of viable preosteoblasts (f); the Alizarin Red S staining of the cells cultured in the extracts of Mg-Zn/10TCP (g) and Mg-Zn/5TCP (h) scaffolds after 21 d of culture; (i) the quantification of ALP (after 14 d of culture) and Alizarin Red S staining (after 21 d of culture).

the control group (Fig. 9i). To study the mineralization level of the specimens, Alizarin Red S staining was conducted at day 21. The presence of calcified matrix indicated that mineralization had occurred in the presence of both Mg-Zn/5TCP and Mg-Zn/10TCP extracts (Fig. 9g and h). The mineralization levels were higher than that of the control group, but there was no statistically significant difference between Mg-Zn/5TCP and Mg-Zn/10TCP (Fig. 9i).

4. Discussion

4.1. Fabrication of the composite scaffolds

4.1.1. Ink preparation

The key to successful extrusion-based 3D printing of Mg scaffolds is the design and preparation of a printable ink with suitable viscoelastic properties. In the case of Mg-based composite scaffolds, the dispersion of micro-sized bioceramic particles in the ink is another critical factor that needs to be carefully considered. We observed that the agglomeration of bioceramic particles greatly affects the flowability of the inks, making the nozzle clog during the printing process (Fig. S1a). Uniform dispersion of bioceramic particles was beneficial both for printing and for improving the final properties of the fabricated composite scaffolds. To obtain inks with optimum β -TCP dispersion, we first studied the dispersion of β -TCP in the binder. The β -TCP distribution was more homogenous

for a higher percentage of the binder (Fig. 2A-(a-c)), indicating that the binder itself could act as a dispersant. Polyisobutylene with hexane is reported to stabilize dispersed particles through steric stabilization [46,47]. In this scenario, an organic layer forms on the surface of the particles, acting as a steric barrier and preventing the particles from coming into direct surface contact [48]. Therefore, to achieve uniform dispersion of β -TCP, the binder should ideally be capable of forming a steric layer on each β -TCP particle. This is why a higher percentage of the binder corresponded to more uniform dispersion of the bioceramic particles.

Furthermore, we found that the dispersion of the β -TCP particles in the inks was largely dependent on that of β -TCP in the binder (*i.e.*, pre-inks, Fig. 2A). At a given ratio of β -TCP to binder (*e.g.*, 97% that reached the best dispersion degree), loading a larger amount of β -TCP in the ink resulted in a larger amount of binder in the prepared ink (*i.e.*, mixtures of β -TCP, binder, and the Mg-Zn powder). For reaching the best dispersion degree, 52 vol.% binder is needed for the Mg-Zn/5TCP ink, 70 vol.% for the Mg-Zn/10TCP ink and 77 vol.% for the Mg-Zn/15TCP ink. On the other hand, too much binder resulted in inks losing their viscoelastic properties, because of the low level of powder loading (*e.g.*, Mg-Zn/10TCP_97% and Mg-Zn/15TCP_97%, Fig. 2B). Therefore, the homogeneity and viscoelasticity of the inks need to be simultaneously considered. Binder is needed for uniform dispersion in the ink, but too much binder makes the ink unprintable. For being able to print, the dis-

persion of β -TCP in the Mg-Zn/10TCP and Mg-Zn/15TCP inks had to be compromised in the present study. Because of a lower percentage of β -TCP loading, the Mg-Zn/5TCP ink showed the best dispersion, while being also printable (Fig. S2d).

In summary, extrusion-based 3D printing has demonstrated significant advantages for the fabrication of composite scaffolds over other AM techniques, because it allows for the fine-tuning of printable inks to optimize the dispersion of micro-sized particles. The binder system should, therefore, be judiciously designed to both possess suitable viscoelastic characteristics and exhibit favorable dispersion behavior. Additional dispersants may be added into the binder system to further improve its dispersion function.

4.1.2. Interfacial bonding between Mg and bioceramic in the composite scaffolds

For the as-sintered composite scaffolds, having sufficiently strong interfacial bonding between the Mg-based matrix and bioceramic reinforcement is crucial both for realizing a strengthening effect and improving their integrity during biodegradation [49]. An effective way to enhance interfacial bonding is to form an interlayer at the Mg/bioceramic interface so as to chemically interlock the constituents [50]. To form an interlayer, two criteria must be met: (i) a thermochemical reaction needs to take place at the Mg/bioceramic interface to form an intermediate layer as a reaction product, and (ii) either the bioceramic elemental atoms diffuse across the Mg oxide layer into Mg or the elemental atoms in the Mg matrix diffuse across the Mg oxide layer out of Mg. It has been found that Mg can react with β -TCP through a solid-state reaction [49,51]. Mg^{2+} and Zn^{2+} have the energetically preferential Ca-5 site in the β -TCP structure for substitution [52]. We could, therefore, take advantage of the reaction between the Mg matrix and the added β -TCP during sintering to enhance the interfacial bonding. However, the original MgO layer on the surface of the Mg powder particle surfaces is quite stable and the diffusion coefficient of Mg atoms (*i.e.*, 5.25×10^{-24} at 650 °C) through the oxide layer is relatively low [53]. Some other studies have used spark plasma sintering to fabricate Mg/ β -TCP composites while applying external pressure during the sintering process to disrupt the oxide layer, thereby facilitating diffusion [49,51]. However, the specific design of our porous scaffolds with a complex 3D structure restricted us from applying external mechanical pressure. Instead, we tried to apply a liquid-phase sintering strategy to facilitate effective diffusion. In this approach, a small volume fraction of liquid is formed during sintering, thereby facilitating the disruption of the oxide layer present on the surface of the powder particles [28]. Because of the faster diffusion of atoms during liquid-state sintering as compared to solid-state sintering and the high diffusivity of Ca in Mg [54], a $\text{Ca}_2\text{Mg}_6\text{Zn}_3$ intermediate layer quickly formed during sintering (Fig. 4A, B and Table 4). It has been found that $\text{Ca}_2\text{Mg}_6\text{Zn}_3$ can form when the Zn/Ca atomic ratio exceeds 1.2 [55]. MgO could form at the interface between the $\text{Ca}_2\text{Mg}_6\text{Zn}_3$ phase and the Mg-Zn matrix as a thin layer (Fig. 3B, but not observable in the microstructure under SEM), because of the high affinity of Mg with O atoms from β -TCP, which also helped enhance the interfacial bonding due to the high stability of MgO.

The diffusion or the reaction stopped when it reached equilibrium. At the area of local agglomerates of β -TCP, the β -TCP particles could not completely react with the surrounding Mg-Zn matrix and, therefore, a small amount of the $\text{Ca}_4\text{P}_2\text{O}$ phase that derived from $\text{Ca}_3(\text{PO}_4)_2$ was left beside the $\text{Ca}_2\text{Mg}_6\text{Zn}_3$ phase (Fig. 3 and Fig. 4). However, the particle-shaped $\text{Ca}_4\text{P}_2\text{O}$ phase had poorer interfacial bonding with the Mg-Zn matrix as compared to the integrated $\text{Ca}_2\text{Mg}_6\text{Zn}_3$ phase, as confirmed by the detachment of the $\text{Ca}_4\text{P}_2\text{O}$ phase during sanding (Fig. 3A-c4).

The addition of a larger amount of β -TCP into the Mg-Zn scaffolds resulted in higher fractions of the $\text{Ca}_2\text{Mg}_6\text{Zn}_3$ and $\text{Ca}_4\text{P}_2\text{O}$

phases. The total volume fractions of these two new phases (*i.e.*, 6.90% for Mg-Zn/5TCP, 11.0% for Mg-Zn/10TCP, and 17.7% for Mg-Zn/15TCP; Table 4) were higher than the design values (*i.e.*, 2.8%, 5.8% and 8.9% β -TCP in volume percentage) because of the diffusion between the Mg-Zn matrix and β -TCP. This was confirmed by EDS mapping (Fig. 4A and B), which also detected the presence of Ca in the Mg matrix.

4.1.3. The fabricated Mg-Zn/TCP composite scaffolds

Previous studies showed that excessive flow of liquid Mg and poor wettability between molten Mg and solid Mg powder particles caused nodules to form on the struts [28,32]. β -TCP has a better wettability with liquid Mg than other bioceramics, such as HA [10]. In this study, the reaction that occurred between the liquid Mg-Zn and β -TCP further promoted the wettability. More liquid Mg-Zn could, therefore, be accommodated in the porous structure, when the scaffolds with a higher β -TCP volume fraction were sintered in the liquid state. This means that a higher temperature could be chosen for sintering the scaffolds with a higher β -TCP percentage to achieve higher densification, while maintaining the fidelity of the struts. For sintering the Mg-Zn/TCP scaffolds, 600 °C could be used for 5% β -TCP, 620 °C for 10% β -TCP, and 640 °C for 15% β -TCP to reach maximum densification. Under the optimized sintering conditions, the relative densities of struts reached 99.9% for the Mg-Zn/5TCP and 99.5% for the Mg-Zn/10TCP composite scaffolds, which were much higher than that for the Mg-Zn scaffolds (Table 2). This confirms that the density of the composite scaffolds in extrusion-based 3D printing can reach and even exceed the levels observed in high laser power PBF AM and in external pressure-assisted powder metallurgy approaches (Table S1). This marks a big step forward in the AM of Mg-based scaffolds, because the high laser power and the risk of explosion can be avoided altogether without having to compromise in terms of the relative density of the struts. This study also sheds light on the design of Mg/bioceramic composite scaffolds with adjusted densification.

The porosity of the struts of Mg-Zn/15TCP specimens was quite high (*i.e.*, $13.9 \pm 4.7\%$). This was because the severe agglomeration of β -TCP particles not only resulted in the generation of voids during 3D printing (Fig. S1a) but also decreased the flowability of the liquid phase formed during liquid-phase sintering.

4.2. Biodegradation behavior

The degradation rate of the Mg-Zn/5TCP composite scaffold (*i.e.*, 0.5 mm/y at day 28) was lower than that of the porous Mg-Zn scaffold without any addition of β -TCP, fabricated by using the same 3D printing technique [32]. This value reached the ideal range of biodegradation rates suggested for bone substitutes (*i.e.*, 0.2–0.5 mm/y) [56]. The biodegradation rate of the Mg-Zn/10TCP specimens (*i.e.*, 0.7 mm/y at day 28) was similar (*i.e.*, 0.7 mm/y and 1.7 mm/y at day 28 and day 7, respectively) to that of the Mg-Zn scaffolds, while the Mg-Zn/15TCP specimens exhibited the highest rate (*i.e.*, 2.3 mm/y at day 7). This means that the addition of a certain amount of β -TCP could help the extrusion-based 3D printed Mg scaffolds reach a desired degradation rate, but adding too much β -TCP adversely affects the corrosion resistance of the scaffolds.

The highly densified Mg-Zn/5TCP struts with fewer open micropores, as compared to the Mg-Zn struts (Table 2), significantly decreased the surface area of the struts for the initiation of biodegradation. This was one of the main reasons for the decreased biodegradation rate of the Mg-Zn/5TCP scaffolds. Moreover, the new phases formed in the Mg-Zn/TCP scaffolds must have influenced the corrosion behavior and corrosion mechanism, since the Mg-Zn/10TCP specimens that possessed highly densified struts

(Table 2) consistently showed higher corrosion rates during the *in vitro* immersion period, as compared to Mg-Zn/5TCP (Fig. 5d).

To reveal the effects of the new phases on the corrosion mechanism of the Mg-Zn/TCP specimens, the degraded specimens (Fig. S11a) were observed under SEM. During the *in vitro* immersion, the corrosion of these specimens was found to have been initiated at the grain boundaries or in the surrounding area of the formed interfacial phases, predominately the $\text{Ca}_2\text{Mg}_6\text{Zn}_3$ phase. The $\text{Ca}_2\text{Mg}_6\text{Zn}_3$ phase has a higher standard electrode potential than the Mg matrix [57]. The Mg-Zn matrix, therefore, degraded in the r-SBF as the anode, while the $\text{Ca}_2\text{Mg}_6\text{Zn}_3$ phase was protected. The $\text{Ca}_2\text{Mg}_6\text{Zn}_3$ phase was quite stable and remained largely unaffected as the Mg-Zn matrix became corroded (Fig. S11a). It was also observed that the corrosion pathway diverted when it met the $\text{Ca}_2\text{Mg}_6\text{Zn}_3$ phase (see the arrows in Fig. S11b), indicating that the $\text{Ca}_2\text{Mg}_6\text{Zn}_3$ phase acted as a temporary local corrosion barrier, blocking the pitting pathway and limiting intense corrosion propagation [58]. Although the generation of the $\text{Ca}_2\text{Mg}_6\text{Zn}_3$ phase was not designed intentionally at the start, its presence in the scaffolds decreased the corrosion rate, while the original β -TCP particles quickly dissolved in the electrolyte, accelerating the corrosion of the specimens [11]. The micro galvanic corrosion and the blocking effect of the $\text{Ca}_2\text{Mg}_6\text{Zn}_3$ phase compete as the Mg-Zn/TCP specimens corrode. In the Mg-Zn/5TCP group, the $\text{Ca}_2\text{Mg}_6\text{Zn}_3$ phase was mainly distributed in a strip-shaped network along the grain boundaries (Fig. 3Aa3 and a4). The associated blocking effect of this phase, thus, dominated the corrosion behavior [55,58], which contributed to the desired biodegradation rate of these specimens. However, the irregular shape of the $\text{Ca}_2\text{Mg}_6\text{Zn}_3$ phase with larger surface areas in the Mg-Zn/10TCP and Mg-Zn/15TCP groups resulted in galvanic corrosion dominating the corrosion response. In addition, the $\text{Ca}_2\text{Mg}_6\text{Zn}_3$ phase, having strong interfacial bonding with the Mg-Zn matrix, could inhibit the electrolyte (*i.e.*, r-SBF) from seeping into the struts, while the poor interfacial bonding between the $\text{Ca}_4\text{P}_2\text{O}$ phase and the Mg-Zn matrix increased the available surface area that directly contacted the electrolyte. Mg-Zn/10TCP and Mg-Zn/15TCP with higher volume fractions of the $\text{Ca}_4\text{P}_2\text{O}$ phase, therefore, had more initiation sites for corrosion in the struts, as compared to Mg-Zn/5TCP at the beginning of *in vitro* immersion.

During *in vitro* degradation, hydrogen was produced through a cathodic reaction, resulting in a local alkaline environment. The alkalinity of the local solution induced the precipitation of the corrosion products. The formation of magnesium hydroxide ($\text{Mg}(\text{OH})_2$) on the surface may act as a protective layer against further corrosion. Although the formation of the stable ZnO phase (Fig. 7 and Fig. S11) might stabilize this corrosion layer [32], $\text{Mg}(\text{OH})_2$ could react with Cl^- in r-SBF, resulting in its dissolution and the generation of cracks in the layer (Fig. S11a). Nevertheless, it was interesting to find out that the stable $\text{Ca}_2\text{Mg}_6\text{Zn}_3$ phase in the corrosion layer could inhibit crack propagation and maintain the integrity of the corrosion layer, thereby providing prolonged protection for the scaffold substrates (arrow in Fig. S11a). Therefore, the corrosion rates of the Mg-Zn/5TCP and Mg-Zn/10TCP groups decreased at the beginning of the *in vitro* degradation and then increased at days 14 and 7 (Fig. 5d), respectively, when the $\text{Ca}_2\text{Mg}_6\text{Zn}_3$ phase fell off. The formed protective layer provided favorable sites for the nucleation and deposition of Ca- and P-containing compounds.

A higher Ca ion concentration was, indeed, detected in the medium collected after the *in vitro* immersion tests of the scaffolds with a higher β -TCP content (Fig. S12), indicating an intensified rate of release of Ca ions from the composite scaffolds. We speculated that Ca ions might be released from the Mg-Zn matrix during the dissolution of the composite scaffolds, since it was found that Ca atoms diffused into the Mg-Zn matrix during sintering and were uniformly distributed there (Fig. 4A and B). During *in*

vitro degradation, with Ca being saturated locally and in the alkaline microenvironment, carbonate and apatite could form and continuously grow on the previously formed protective layer, as mentioned above. The presence of a notable number of Mg ions could inhibit the HA formation, but it could also stabilize more acidic hydrated apatite compounds, such as brushite [59,60]. That is why brushite was detected on the biodegraded scaffolds during degradation. After 14 d of biodegradation, brushite was difficult to be detected and the corrosion products were mainly $\text{Mg}(\text{OH})_2$ (Fig. 7 and S9). This could be because the $\text{PO}_4^{2-}/\text{HPO}_4^-$ ions in the surrounding solution had been exhausted by forming apatite compounds, while $\text{Mg}(\text{OH})_2$ and CaCO_3 continued to be deposited.

Having discussed the biodegradation behavior of the composite scaffolds at the micro level, it is important to consider the macro-scale mechanisms as well. Despite the benefits of a porous structure in allowing bone ingrowth, it remains a major challenge to introduce porosity into a Mg-based material, given that it increases its corrosion rate as compared to a bulk Mg counterpart [61–67] due to the increase in surface area. In this study, however, the *in vitro* biodegradation rates of the all three groups of Mg-Zn/TCP (*i.e.*, 0.5–2.3 mm/y, porosity: 48%–55%) were lower than or similar to those of near-bulk materials with similar compositions (*i.e.*, 0.6–15 mm/y [68–72]). Unlike other traditional manufacturing techniques [68–72] and the recently reported binder jet AM technique [62], extrusion-based 3D printing technique allows for the fabrication of geometrically ordered porous Mg structures, which could then be used to adjust the biodegradation behavior of the scaffolds. The structures featured in this study were furnished with struts that had an angle of 90° at their intersections, which limited the diffusion of Mg^{2+} and OH^- ions, especially in the central region of the scaffolds. The corrosion products, including $\text{Mg}(\text{OH})_2$, ZnO and brushite, formed immediately between the struts in the local alkaline environment (Fig. 6, S5 and S7). Given the stability of the corrosion products, as mentioned above, and the limited flowability of the electrolyte, the formed corrosion products were entrapped inside the scaffolds (Fig. 5a, S3a and S4a), leading to an increase in the total volume of the scaffolds (including the volume of biodegradation products) and a decrease in porosity (Fig. 5, S3 and S4) during most of the *in vitro* degradation period. The entrapped corrosion products in the pores of the scaffolds acted as a highly protective barrier, and also helped maintain the integrity of the scaffolds, thereby inhibiting the further progress of the corrosion process. Therefore, the scaffolds showed a relatively low rate of biodegradation and a decreasing trend with the immersion time (Fig. 5d). On the other hand, the accumulation of the corrosion products between the struts created narrow spaces where crevice-like corrosion might occur, accelerating the corrosion at the center of the scaffolds. Therefore, more severe corrosion was found in the central area as compared to the periphery (Fig. 5a, S4a and S5a). These results indicate that the design of open porous structures is of great importance in tailoring the biodegradation behavior of Mg-based materials.

4.3. Mechanical behavior

When choosing the strain rate for compression test, the effect of strain rate on the mechanical responses should be considered. The strain-hardening effect has indeed been found in some metallic materials, such as Ti [73,74] and Mg [75]. At a standardized strain rate, the strain-hardening effect can be minimized in highly porous structure [76]. According to the standard ISO 13,314: 2011, the initial compression strain rate should be between 10^{-3} and 10^{-2} s^{-1} . Therefore, for the highly porous Mg-Zn/TCP scaffold specimens with a height of 12 mm, a crosshead speed of 2 mm/min (corresponding to an initial strain rate of 0.003 s^{-1}) was chosen.

The uniaxial compressive stress-strain curves of the Mg-Zn/TCP specimens were similar to those of extrusion-based 3D printed Mg-Zn scaffolds [32], starting with an initial elastic stage and followed by a strain-hardening stage (Fig. 8). The yield strengths and Young's moduli of all the three groups of the Mg-Zn/TCP composite scaffolds were higher than those of the previously reported Mg-Zn scaffolds [32]. Remarkably, the yield strengths of the Mg-Zn/5TCP and Mg-Zn/10TCP composite scaffolds were about two times as high as the yield strength of the Mg-Zn scaffolds. First, the significant enhancements in strength could be attributed to the strong interfacial bonding between the Mg-Zn matrix and $\text{Ca}_2\text{Mg}_6\text{Zn}_3$ phase, and the higher nanohardness of the newly formed phases (55.1 GPa) as compared with the nanohardness of the Mg-Zn matrix (43.0 GPa). The load could, therefore, be effectively transferred from the Mg-based matrix to the second phase [77]. Second, the presence of the well-dispersed, micro-sized $\text{Ca}_4\text{P}_2\text{O}$ phase in the Mg-Zn matrix may act as obstacles to dislocation movement, thereby strengthening the scaffolds [78]. On the other hand, the $\text{Ca}_4\text{P}_2\text{O}$ phase with an irregular shape may also act as a crack initiation site when the specimens are (dynamically) loaded. Third, almost fully dense struts of Mg-Zn/5TCP and Mg-Zn/10TCP could withstand higher loads during the mechanical tests while largely avoiding the stress concentrations that result from micropores in the struts. In Mg-Zn/15TCP, the presence of large clusters of $\text{Ca}_4\text{P}_2\text{O}$ as well as voids adversely affected its mechanical properties, leading to a lower yield strength and lower toughness (Supplementary file).

Bone substitutes should continue to provide sufficient mechanical support as *in vivo* biodegradation progresses and before the newly formed bone can take over. Understanding the time-dependent evolution of the mechanical properties of biodegradable biomaterials is, therefore, of great importance. The Mg-Zn/TCP specimens developed here exhibited bone-mimicking mechanical properties during the *in vitro* degradation process, reaching the range of the trabecular bone (*i.e.*, yield strength = 0.2 – 80 MPa; Young's modulus = 10 – 2000 MPa) [64]. After 14 d of *in vitro* degradation, the Mg-Zn/5TCP scaffolds could still match the strength of the femoral cancellous bone (15 MPa) [79,80], indicating that these scaffolds could provide enough mechanical support for treating the femoral nonunion. The mechanical properties of Mg-Zn/5TCP and Mg-Zn/10TCP fluctuated during the *in vitro* degradation (Fig. 8b and c), which is likely due to the competition between the dissolution of the scaffolds which leads to a decreased strength value and the formation of corrosion products that increases the strength value [32]. The corrosion products could be considered as an additional reinforcing phase at the beginning of the immersion in r-SBF (*i.e.*, the first 7 days) when the interfacial bonding between the substrate and corrosion products is still strong. Our results show that the corrosion products could not be disintegrated when they formed in the center area of the composite scaffolds, therefore, most of the $\text{Ca}_2\text{Mg}_6\text{Zn}_3$ phase still stayed in the original area of the struts surrounded by the corrosion products (Fig. S11a), further contributing to strengthening the composite scaffolds. Furthermore, the formation of the corrosion products filling the micropores and the space between the struts led to a decrease in the porosity of the specimens (Fig. 5), which translates to higher mechanical properties. After 14 d of biodegradation, the Mg-Zn/10TCP specimens showed a lower yield strength and Young's modulus than the Mg-Zn/5TCP specimens, because the higher corrosion rate of the former resulted in a larger loss of Mg as the *in vitro* degradation processes progressed (Fig. 5b).

4.4. Biological response

Cellular adhesion is a prerequisite for cell proliferation and osteogenic differentiation [77]. The cell adhesion assay was per-

formed by seeding preosteoblasts directly on the fabricated scaffolds. The well-spread morphology of the cells and the increased number of viable cells during the first week of culture demonstrated that the Mg-Zn/5TCP and Mg-Zn/10TCP scaffolds supported the adhesion and proliferation of the cells as compared to the Mg-Zn scaffolds. Although the original β -TCP phase was not found in the as-sintered Mg-Zn/TCP composite scaffolds anymore, the addition of β -TCP into the Mg-Zn scaffolds was still effective in improving the early cell response. First, the Mg-Zn/TCP composite scaffolds released less zinc ions when they were immersed in the cell culture medium (Fig. S12). It has been shown that a too high concentration of Zn^{2+} inhibits the growth of preosteoblast, while a low concentration promotes the viability, proliferation, and migration of osteoblasts [81]. Part of the zinc originally presents in the Mg matrix or in the MgZn_2 secondary phase of the Mg-Zn scaffolds was consumed for generating a more stable phase (*i.e.*, $\text{Ca}_2\text{Mg}_6\text{Zn}_3$) in the Mg-Zn/TCP composite scaffolds. As discussed above, the $\text{Ca}_2\text{Mg}_6\text{Zn}_3$ phase did not degrade or dissolve during the immersion tests, meaning that a limited number of zinc ions were released from this phase. Consequently, while the degradation rates of Mg-Zn/5TCP and Mg-Zn/10TCP were similar to that of Mg-Zn, a smaller number of Zn^{2+} ions were released from those groups. Second, the formation of brushite on the scaffolds during initial biodegradation could stimulate cell proliferation and differentiation *in vitro* and promote the regeneration of vascularized bone *in vivo* [82]. After 14 d, however, both Mg-Zn/5TCP and Mg-Zn/10TCP showed cell growth inhibition (Fig. 9f). This is likely due to the increasing numbers of Mg, $\text{Ca}_4\text{P}_2\text{O}$, and $\text{Ca}_2\text{Mg}_6\text{Zn}_3$ particles that became disintegrated from the scaffolds could affect the cell response. Such submicron-sized particles are known to induce cytotoxicity in various cell lines [83]. In addition, the brushite layer was found to be covered by a $\text{Mg}(\text{OH})_2$ layer at the later time points, which could reduce bioactivity on the surfaces of the specimens. In an earlier *in vivo* study [11], a dense Mg-Zn/10 wt.% β -TCP composite material (*in vitro* biodegradation rate: 15.9 mm/y) was implanted into rabbits to evaluate its biocompatibility. It was found that the Mg^{2+} , Zn^{2+} , and Ca^{2+} ions could be metabolized in the blood with no adverse effects on the kidney, liver, or heart. As compared to the dense Mg-Zn/10 wt.% β -TCP material mentioned above, the Mg-Zn/TCP specimens developed here had much lower biodegradation rates, which would undoubtedly be also safe for the visceral organs if being implanted in animals.

The influences of the extracts from the Mg-Zn/5TCP and Mg-Zn/10TCP composite scaffolds on the osteogenic differentiation and mineralization of preosteoblasts were evaluated by ALP and Alizarin Red S assays, respectively (Fig. 9g-i). Both extracts exhibited a clear effect on promoting the osteogenic differentiation and matrix mineralization, which could be because the appropriate concentrations of the released Mg, Zn, and Ca ions activated specific signaling pathways, stimulating mineralization [84–86]. The human body can regulate ion concentrations in the local environment through active transport processes, and both the degradation rate and surface condition of the scaffolds may change in a more complex microenvironment *in vivo*. *In vivo* studies should, therefore, be performed on the extrusion-based 3D printed Mg-Zn/TCP specimens to better understand their biological responses.

5. Conclusions

1. We fabricated porous Mg-Zn/x β -TCP ($x = 5, 10$ and 15 wt.%) composite scaffolds by using an extrusion-based 3D printing technique for the first time. The ink formulations were optimized to balance the homogeneity of bioceramic particles with appropriate viscoelastic properties and, thus, printability. The dispersion of β -TCP particles in the Mg-Zn/5TCP inks and the resulting scaffolds were the most uniform.

2. The relative densities of the materials making up the struts were higher than 99% in the Mg-Zn/5TCP and Mg-Zn/10TCP specimens, reaching the level usually only achieved through PBF AM.

3. The Mg-Zn/5TCP specimens showed a decreased *in vitro* rate of biodegradation (i.e., 0.5 mm/y) as compared with Mg-Zn. This rate falls within the desired range of biodegradation rates for ideal bone substitutes. As for the Mg-Zn/15TCP specimens, the inhomogeneous dispersion of β -TCP particles deteriorated their biodegradation behavior.

4. The yield strengths of the Mg-Zn/5TCP and Mg-Zn/10TCP composite scaffolds were about two times as high as the yield strength of the Mg-Zn scaffolds. The mechanical properties of the composite scaffolds fluctuated over the biodegradation period of 28 d, but the strengths and elastic moduli remained in the range of the mechanical properties of the cancellous bone.

5. The direct cultures of preosteoblasts on the Mg-Zn/5TCP and Mg-Zn/10TCP specimens showed their significantly improved cytocompatibility, as compared to Mg-Zn after 7 d. The ALP activity in the indirect culture was significantly higher for the composites as compared to the control group (i.e., the Mg-Zn alloy).

The results obtained clearly show that the Mg-based composite scaffolds developed in this study satisfy most of the requirements of ideal bone substitutes and should be further developed towards potential clinical application.

Declaration of Competing Interest

The authors declare that they have no known competing financial interests or personal relationships that could have appeared to influence the work reported in this paper.

Acknowledgments

J.D. thanks the China Scholarship Council (CSC) for financial support. Mr. Ruud Hendriks at the Department of Materials Science and Engineering, Delft University of Technology, is acknowledged for the XRD analysis. Mr. Michel van den Brink at the Department of Process and Energy, Delft University of Technology, is acknowledged for the ICP-OES analysis. Mr. Arjan Thijssen at the Faculty of Civil Engineering and Geosciences, Delft University of Technology, is acknowledged for μ CT scans.

Supplementary materials

Supplementary material associated with this article can be found, in the online version, at [doi:10.1016/j.actbio.2022.08.002](https://doi.org/10.1016/j.actbio.2022.08.002).

References

- Q. Zhang, W. Zhang, Z. Zhang, L. Zhang, H. Chen, M. Hao, J. Deng, P. Tang, Femoral nonunion with segmental bone defect treated by distraction osteogenesis with monolateral external fixation, *J. Orthop. Surg. Res.* 12 (2017) 183.
- L. Ye, J. Xu, J. Mi, X. He, Q. Pan, L. Zheng, H. Zu, Z. Chen, B. Dai, X. Li, Q. Pang, L. Zou, L. Zhou, L. Huang, W. Tong, G. Li, L. Qin, Biodegradable magnesium combined with distraction osteogenesis synergistically stimulates bone tissue regeneration via CGRP-FAK-VEGF signaling axis, *Biomaterials* 275 (2021) 120984.
- F. Witte, The history of biodegradable magnesium implants: a review, *Acta Biomater.* 6 (2010) 1680–1692.
- L.H.N. Dang, Y.K. Kim, S.Y. Kim, K.J. Lim, K. Bode, M.H. Lee, K.B. Lee, Radiographic and histologic effects of bone morphogenetic protein-2/hydroxyapatite within bioabsorbable magnesium screws in a rabbit model, *J. Orthop. Surg. Res.* 14 (2019) 117.
- V.K. Bommala, M.G. Krishna, C.T. Rao, Magnesium matrix composites for biomedical applications: a review, *J. Magnes. Alloy.* 7 (2019) 72–79.
- M. Shahin, K. Munir, C. Wen, Y. Li, Magnesium matrix nanocomposites for orthopedic applications: a review from mechanical, corrosion, and biological perspectives, *Acta Biomater.* 96 (2019) 1–19.
- R. Radha, D. Sreekanth, Insight of magnesium alloys and composites for orthopedic implant applications - A review, *J. Magnes. Alloy.* 5 (2017) 286–312.
- S. Shadanbaz, G.J. Dias, Calcium phosphate coatings on magnesium alloys for biomedical applications: a review, *Acta Biomater.* 8 (2012) 20–30.
- H. Hornberger, S. Virtanen, A.R. Boccaccini, Biomedical coatings on magnesium alloys - a review, *Acta Biomater.* 8 (2012) 2442–2455.
- K. Kusnierczyk, M. Basista, Recent advances in research on magnesium alloys and magnesium-calcium phosphate composites as biodegradable implant materials, *J. Biomater. Appl.* 31 (2017) 878–900.
- K. Yu, L.J. Chen, J. Zhao, S.J. Li, Y.L. Dai, Q. Huang, Z.M. Yu, *In vitro* corrosion behavior and *in vivo* biodegradation of biomedical β -Ca₃(PO₄)₂/Mg-Zn composites, *Acta Biomater.* 8 (2012) 2845–2855.
- X.L. Ma, L.H. Dong, X. Wang, Microstructure, mechanical property and corrosion behavior of co-continuous β -TCP/MgCa composite manufactured by suction casting, *Mater. Des.* 56 (2014) 305–312.
- X. Wang, L.H. Dong, J.T. Li, X.L. Li, X.L. Ma, Y.F. Zheng, Microstructure, mechanical property and corrosion behavior of interpenetrating (HA+ β -TCP)/MgCa composite fabricated by suction casting, *Mater. Sci. Eng. C-Mater. Biol. Appl.* 33 (2013) 4266–4273.
- H.R. Zheng, Z. Li, C. You, D.B. Liu, M.F. Chen, Effects of MgO modified β -TCP nanoparticles on the microstructure and properties of β -TCP/Mg-Zn-Zr composites, *Bioact. Mater.* 2 (2017) 1–9.
- D.B. Liu, Y.B. Zuo, W.Y. Meng, M.F. Chen, Z. Fan, Fabrication of biodegradable nano-sized β -TCP/Mg composite by a novel melt shearing technology, *Mater. Sci. Eng. C-Mater. Biol. Appl.* 32 (2012) 1253–1258.
- Z. Cui, Y. Zhang, Y. Cheng, D. Gong, W. Wang, Microstructure, mechanical, corrosion properties and cytotoxicity of betacalcium polyphosphate reinforced ZK61 magnesium alloy composite by spark plasma sintering, *Mater. Sci. Eng. C-Mater. Biol. Appl.* 99 (2019) 1035–1047.
- Y. Zhang, H. Yang, S. Lei, S. Zhu, J. Wang, Y. Sun, S. Guan, Preparation of biodegradable Mg/ β -TCP biofunctional gradient materials by friction stir processing and pulse reverse current electrodeposition, *Acta Metall. Sin.-Engl. Lett.* 33 (2019) 103–114.
- A.A. Zadpoor, Bone tissue regeneration: the role of scaffold geometry, *Biomater. Sci.* 3 (2015) 231–245.
- Y. Li, P. Pavanram, J. Zhou, K. Lietaert, P. Taheri, W. Li, H. San, M.A. Leeflang, J.M.C. Mol, H. Jahr, A.A. Zadpoor, Additively manufactured biodegradable porous zinc, *Acta Biomater.* 101 (2020) 609–623.
- A. Zadpoor, Current trends in metallic orthopedic biomaterials: from additive manufacturing to bio-functionalization, infection prevention, and beyond, *Int. J. Mol. Sci.* 19 (2018) 2684.
- A.P. Moreno Madrid, S.M. Vrech, M.A. Sanchez, A.P. Rodriguez, Advances in additive manufacturing for bone tissue engineering scaffolds, *Mater. Sci. Eng. C-Mater. Biol. Appl.* 100 (2019) 631–644.
- Y. Zamani, H. Ghazanfari, G. Erabi, A. Moghani, B. Fakić, S.M. Hosseini, B.P.M. Fakić, A review of additive manufacturing of Mg-based alloys and composite implants, *J. Compos. Compd.* 2 (2021) 71–83.
- Y. Yin, Q. Huang, L. Liang, X. Hu, T. Liu, Y. Weng, T. Long, Y. Liu, Q. Li, S. Zhou, H. Wu, *In vitro* degradation behavior and cytocompatibility of ZK30/bioactive glass composites fabricated by selective laser melting for biomedical applications, *J. Alloys Compd.* 785 (2019) 38–45.
- C.J. Shuai, Y.Z. Zhou, Y.W. Yang, P. Feng, L. Liu, C.X. He, M.C. Zhao, S. Yang, C.D. Gao, P. Wu, Biodegradation resistance and bioactivity of hydroxyapatite enhanced Mg-Zn composites via selective laser melting, *Materials (Basel)* 10 (2017) 307–319.
- Y. Yang, C. Lu, L. Shen, Z. Zhao, S. Peng, C. Shuai, In-situ deposition of apatite layer to protect Mg-based composite fabricated via laser additive manufacturing, *J. Magnes. Alloy* (2021) in press.
- Y. Yang, C. Lu, S. Peng, L. Shen, D. Wang, F. Qi, C. Shuai, Laser additive manufacturing of Mg-based composite with improved degradation behaviour, *Virtual Phys. Prototy.* 15 (2020) 278–293.
- Y. Li, J. Zhou, P. Pavanram, M.A. Leeflang, L.I. Fockaert, B. Pouran, N. Tümer, K.U. Schroder, J.M.C. Mol, H. Weinans, H. Jahr, A.A. Zadpoor, Additively manufactured biodegradable porous magnesium, *Acta Biomater.* 67 (2018) 378–392.
- J. Dong, Y. Li, P. Lin, M.A. Leeflang, S. Van Asperen, K. Yu, N. Tümer, B. Norder, A.A. Zadpoor, J. Zhou, Solvent-cast 3D printing of magnesium scaffolds, *Acta Biomater.* 114 (2020) 497–514.
- H.S. Ma, T. Li, Z.G. Huan, M. Zhang, Z.Z. Yang, J.W. Wang, J. Chang, C.T. Wu, 3D printing of high-strength bioscaffolds for the synergistic treatment of bone cancer, *NPG Asia Mater.* 10 (2018) 31–44.
- J. Li, C. Deng, W. Liang, F. Kang, Y. Bai, B. Ma, C. Wu, S. Dong, Mn-containing bioceramics inhibit osteoclastogenesis and promote osteoporotic bone regeneration via scavenging ROS, *Bioact. Mater.* 6 (2021) 3839–3850.
- J. Dong, N. Tümer, N.E. Putra, J. Zhu, Y. Li, M.A. Leeflang, P. Taheri, L.E. Fratila-Apachitei, J.M.C. Mol, A.A. Zadpoor, J. Zhou, Extrusion-based 3D printed magnesium scaffolds with multifunctional MgF₂ and MgF₂-CaP coatings, *Biomater. Sci.* (2021).
- J. Dong, N. Tümer, M.A. Leeflang, P. Taheri, L.E. Fratila-Apachitei, J.M.C. Mol, A.A. Zadpoor, J. Zhou, Extrusion-based additive manufacturing of Mg-Zn alloy scaffolds, *J. Magnes. Alloy.* (2021) in press.
- F. Khorashadizade, S. Abazari, M. Rajabi, H.R. Bakhsheshi-Rad, A.F. Ismail, S. Sharif, S. Ramakrishna, F. Berto, Overview of magnesium-ceramic composites: mechanical, corrosion and biological properties, *J. Mater. Res. Technol.* 15 (2021) 6034–6066.
- G. Parande, V. Manakari, H. Gupta, M. Gupta, Magnesium- β -tricalcium phosphate composites as a potential orthopedic implant: a mechanical/damping/immersion perspective, *Metals (Basel)* 8 (2018) 343–360.
- Y. Wang, Z. Wu, H. Zhou, Z. Liao, H. Zhang, Corrosion properties in a simulated body fluid of Mg/ β -TCP composites prepared by powder metallurgy, *Int. J. Miner. Metall.* 19 (2012) 1040–1044.

- [36] R. Del Campo, B. Savoini, A. Munoz, M.A. Monge, G. Garces, Mechanical properties and corrosion behavior of Mg-HAP composites, *J. Mech. Behav. Biomed. Mater.* 39 (2014) 238–246.
- [37] M. Rashad, F. Pan, A. Tang, M. Asif, S. Hussain, J. Gou, J. Mao, Improved strength and ductility of magnesium with addition of aluminum and graphene nanoplatelets (Al+GNPs) using semi powder metallurgy method, *J. Ind. Eng. Chem.* 23 (2015) 243–250.
- [38] M. Rashad, F. Pan, A. Tang, Y. Lu, M. Asif, S. Hussain, J. She, J. Gou, J. Mao, Effect of graphene nanoplatelets (GNPs) addition on strength and ductility of magnesium-titanium alloys, *J. Magnes. Alloy.* 1 (2013) 242–248.
- [39] M. Rashad, F. Pan, H. Hu, M. Asif, S. Hussain, J. She, Enhanced tensile properties of magnesium composites reinforced with graphene nanoplatelets, *Mater. Sci. Eng. A-Struct. Mater. Prop. Microstruct. Process.* 630 (2015) 36–44.
- [40] D.B. Liu, Y. Huang, P.B. Prangnell, Microstructure and performance of a biodegradable Mg-1Ca-2Zn-ITCP composite fabricated by combined solidification and deformation processing, *Mater. Lett.* 82 (2012) 7–9.
- [41] Y. Huang, D.B. Liu, L. Anguilano, C. You, M.F. Chen, Fabrication and characterization of a biodegradable Mg-2Zn-0.5Ca/1 beta-TCP composite, *Mater. Sci. Eng. C-Mater. Biol. Appl.* 54 (2015) 120–132.
- [42] G.A. Yakaboylu, E.M. Sabolsky, Determination of a homogeneity factor for composite materials by a microstructural image analysis method, *J. Microsc.* 266 (2017) 263–272.
- [43] N. Barekar, S. Tzamtzis, B.K. Dhindaw, J. Patel, N.Hari Babu, Processing of aluminum-graphite particulate metal matrix composites by advanced shear technology, *J. Mater. Eng. Perform.* 18 (2009) 1230–1240.
- [44] V. Karageorgiou, D. Kaplan, Porosity of 3D biomaterial scaffolds and osteogenesis, *Biomaterials* 26 (2005) 5474–5491.
- [45] A. Oyane, Hyun. Kim, T. Furuya, T. Kokubo, T. Miyazaki, T. Nakamura, Preparation and assessment of revised simulated body fluids, *J. Biomed. Mater. Res. Part A.* 65A (2003) 188–195.
- [46] D.H. Napper, Steric stabilization, *J. Colloid Interface Sci.* 58 (1977) 390–407.
- [47] Melvin D. Croucher, M.L. Hair, Effect of free volume on the steric stabilization of nonaqueous latex dispersions, *J. Colloid Interface Sci.* 81 (1981) 257–265.
- [48] S. Elbasuney, Sustainable steric stabilization of colloidal titania nanoparticles, *Appl. Surf. Sci.* 409 (2017) 438–447.
- [49] K. Narita, E. Kobayashi, T. Sato, Sintering behavior and mechanical properties of magnesium/beta-tricalcium phosphate composites sintered by spark plasma sintering, *Mater. Trans.* 57 (2016) 1620–1627.
- [50] S. Naddafdezfuli, J.C. Brouwer, J.M.C. Mol, F.C.T. Van Der Helm, J. Zhou, Biodegradation and mechanical behavior of an advanced bioceramic-containing Mg matrix composite synthesized through in-situ solid-state oxidation, *J. Mech. Behav. Biomed. Mater.* 80 (2018) 209–221.
- [51] K. Narita, S. Hiromoto, E. Kobayashi, T. Sato, Effects of incorporating β -tricalcium phosphate with reaction sintering into Mg-based composites on degradation and mechanical integrity, *Metals (Basel)* 11 (2021) 227–243.
- [52] K. Matsunaga, T. Kubota, K. Toyoura, A. Nakamura, First-principles calculations of divalent substitution of Ca(2+) in tricalcium phosphates, *Acta Biomater.* 23 (2015) 329–337.
- [53] M. Salehi, S. Maleksaeedi, M.a.B. Sapari, M.L.S. Nai, G.K. Meenashisundaram, M. Gupta, Additive manufacturing of magnesium-zinc-zirconium (ZK) alloys via capillary-mediated binderless three-dimensional printing, *Mater. Des.* 169 (2019) 107683.
- [54] G. Levi, S. Avraham, A. Zilberov, M. Bamberger, Solidification, solution treatment and age hardening of a Mg-1.6wt.% Ca-3.2wt.% Zn alloy, *Acta Mater.* 54 (2006) 523–530.
- [55] P. Jiang, C. Blawert, M.L. Zheludkevich, The corrosion performance and mechanical properties of Mg-Zn based alloys—a review, *Corros. Mater. Degrad.* 1 (2020) 92–158.
- [56] C. Gao, M. Yao, S. Li, P. Feng, S. Peng, C. Shuai, Highly biodegradable and bioactive Fe-Pd-bredigite biocomposites prepared by selective laser melting, *J. Adv. Res.* 20 (2019) 91–104.
- [57] H. Li, S. Qin, Y. Ma, J. Wang, Y. Liu, J. Zhang, Effects of Zn content on the microstructure and the mechanical and corrosion properties of as-cast low-alloyed Mg-Zn-Ca alloys, *Int. J. Miner. Metall.* 25 (2018) 800–809.
- [58] D. Zander, N.A. Zumdieck, Influence of Ca and Zn on the microstructure and corrosion of biodegradable Mg-Ca-Zn alloys, *Corros. Sci.* 93 (2015) 222–233.
- [59] Q. Dong, X. Zhou, Y. Feng, K. Qian, H. Liu, M. Lu, C. Chu, F. Xue, J. Bai, Insights into self-healing behavior and mechanism of dicalcium phosphate dihydrate coating on biomedical Mg, *Bioact. Mater.* 6 (2021) 158–168.
- [60] M.H. Salimi, J.C. Heughebaert, G.H. Nancollas, Crystal growth of calcium phosphates in the presence of magnesium ions, *Langmuir* 1 (1985) 119–122.
- [61] E. Aghion, Y. Perez, Effects of porosity on corrosion resistance of Mg alloy foam produced by powder metallurgy technology, *Mater. Charact.* 96 (2014) 78–83.
- [62] K.X. Kuah, D.J. Blackwood, W.K. Ong, M. Salehi, H.L. Seet, M.L.S. Nai, S. Wijesinghe, Analysis of the corrosion performance of binder jet additive manufactured magnesium alloys for biomedical applications, *J. Magnes. Alloy.* (2021) in press.
- [63] J. Capek, D. Vojtech, Properties of porous magnesium prepared by powder metallurgy, *Mater. Sci. Eng. C-Mater. Biol. Appl.* 33 (2013) 564–569.
- [64] M. Yazdimamaghani, M. Razavi, D. Vashae, K. Moharamzadeh, A.R. Boccaccini, L. Tayebi, Porous magnesium-based scaffolds for tissue engineering, *Mater. Sci. Eng. C-Mater. Biol. Appl.* 71 (2017) 1253–1266.
- [65] M.Q. Cheng, T. Wahafu, G.F. Jiang, W. Liu, Y.Q. Qiao, X.C. Peng, T. Cheng, X.L. Zhang, G. He, X.Y. Liu, A novel open-porous magnesium scaffold with controllable microstructures and properties for bone regeneration, *Sci. Rep.* 6 (2016) 24134.
- [66] H.Y. Zhuang, Y. Han, A.L. Feng, Preparation, mechanical properties and *in vitro* biodegradation of porous magnesium scaffolds, *Mater. Sci. Eng. C-Mater. Biol. Appl.* 28 (2008) 1462–1466.
- [67] R. Zeng, W. Dietzel, F. Witte, N. Hort, C. Blawert, Progress and challenge for magnesium alloys as biomaterials, *Adv. Eng. Mater.* 10 (2008) B3–B14.
- [68] D. Liu, G. Xu, S.S. Jamali, Y. Zhao, M. Chen, T. Jurak, Fabrication of biodegradable HA/Mg-Zn-Ca composites and the impact of heterogeneous microstructure on mechanical properties, *in vitro* degradation and cytocompatibility, *Bioelectrochemistry* 129 (2019) 106–115.
- [69] Z. Cui, W. Li, L. Cheng, D. Gong, W. Cheng, W. Wang, Effect of nano-HA content on the mechanical properties, degradation and biocompatible behavior of Mg-Zn/HA composite prepared by spark plasma sintering, *Mater. Charact.* 151 (2019) 620–631.
- [70] Y. Deng, Y. Yang, C. Gao, P. Feng, W. Guo, C. He, J. Chen, C. Shuai, Mechanism for corrosion protection of beta-TCP reinforced ZK60 via laser rapid solidification, *Int. J. Bioprinting.* 4 (2018) 124.
- [71] Y. Yan, Y. Kang, D. Li, K. Yu, T. Xiao, Y. Deng, H. Dai, Y. Dai, H. Xiong, H. Fang, Improvement of the mechanical properties and corrosion resistance of biodegradable beta-Ca3(PO4)2/Mg-Zn composites prepared by powder metallurgy: the adding beta-Ca3(PO4)2, hot extrusion and aging treatment, *Mater. Sci. Eng. C-Mater. Biol. Appl.* 74 (2017) 582–596.
- [72] Q. Yuan, Y. Huang, D. Liu, M. Chen, Effects of solidification cooling rate on the corrosion resistance of a biodegradable beta-TCP/Mg-Zn-Ca composite, *Bioelectrochemistry* 124 (2018) 93–104.
- [73] S.L. Sing, W.Y. Yeong, F.E. Wiria, B.Y. Tay, Characterization of titanium lattice structures fabricated by selective laser melting using an adapted compressive test method, *Exp. Mech.* 56 (2016) 735–748.
- [74] C. Chang, J. Huang, X. Yan, Q. Li, M. Liu, S. Deng, J. Gardan, R. Bolot, M. Chemkhi, H. Liao, Microstructure and mechanical deformation behavior of selective laser melted Ti6Al4V ELI alloy porous structures, *Mater. Lett.* (2020) 277.
- [75] S.M. Chowdhury, D.L. Chen, S.D. Bhole, X. Cao, E. Powidajko, D.C. Weckman, Y. Zhou, Tensile properties and strain-hardening behavior of double-sided arc welded and friction stir welded AZ31B magnesium alloy, *Mater. Sci. Eng.: A* 527 (2010) 2951–2961.
- [76] N. Zou, Q. Li, Mechanical properties of lightweight porous magnesium processed through powder metallurgy, *JOM* 70 (2018) 650–655.
- [77] edited by H. Dieringa, Applications: magnesium-based metal matrix composites (MMCs), in: Mihriban Pekguleryuz, Karl Kainer, Arslan Kaya (Eds.), Fundamentals of Magnesium Alloy Metallurgy, 2013, pp. 317–341, edited by.
- [78] A.L. Feng, Y. Han, Mechanical and *in vitro* degradation behavior of ultrafine calcium polyphosphate reinforced magnesium-alloy composites, *Mater. Des.* 32 (2011) 2813–2820.
- [79] E. Perilli, M. Baleani, C. Ohman, R. Fognani, F. Baruffaldi, M. Viceconti, Dependence of mechanical compressive strength on local variations in microarchitecture in cancellous bone of proximal human femur, *J. Biomech.* 41 (2008) 438–446.
- [80] A. Liu, M. Sun, H. Shao, X. Yang, C. Ma, D. He, Q. Gao, Y. Liu, S. Yan, S. Xu, Y. He, J. Fu, Z. Gou, The outstanding mechanical response and bone regeneration capacity of robocast dilute magnesium-doped wollastonite scaffolds in critical size bone defects, *J. Mater. Chem. B* 4 (2016) 3945–3958.
- [81] H. Yang, B. Jia, Z. Zhang, X. Qu, G. Li, W. Lin, D. Zhu, K. Dai, Y. Zheng, Alloying design of biodegradable zinc as promising bone implants for load-bearing applications, *Nat. Commun.* 11 (2020) 401.
- [82] W. Wang, G. Jia, Q. Wang, H. Huang, X. Li, H. Zeng, W. Ding, F. Witte, C. Zhang, W. Jia, G. Yuan, The *in vitro* and *in vivo* biological effects and osteogenic activity of novel biodegradable porous Mg alloy scaffolds, *Mater. Des.* 189 (2020) 108514.
- [83] A.L. Di Virgilio, M. Reigosa, M.F. De Mele, Biocompatibility of magnesium particles evaluated by *in vitro* cytotoxicity and genotoxicity assays, *J. Biomed. Mater. Res. Part B.* 99 (2011) 111–119.
- [84] D. Li, D. Zhang, Q. Yuan, L. Liu, H. Li, L. Xiong, X. Guo, Y. Yan, K. Yu, Y. Dai, T. Xiao, Y. Li, C. Wen, *In vitro* and *in vivo* assessment of the effect of biodegradable magnesium alloys on osteogenesis, *Acta Biomater.* 141 (2021) 454–465.
- [85] Y. Yu, K. Liu, Z. Wen, W. Liu, L. Zhang, J. Su, Double-edged effects and mechanisms of Zn2+ microenvironments on osteogenic activity of BMSCs: osteogenic differentiation or apoptosis, *RSC Adv.* 10 (2020) 14915–14927.
- [86] H. Gu, F. Guo, X. Zhou, L. Gong, Y. Zhang, W. Zhai, L. Chen, L. Cen, S. Yin, J. Chang, L. Cui, The stimulation of osteogenic differentiation of human adipose-derived stem cells by ionic products from akermanite dissolution via activation of the ERK pathway, *Biomaterials* 32 (2011) 7023–7033.